Environmental Science Advances

ROYAL SOCIETY OF CHEMISTRY

PAPER

View Article Online
View Journal | View Issue

Cite this: *Environ. Sci.: Adv.*, 2024, **3**, 480

Hydrophobic ionic liquid (IL)-based magnetic adsorbents: the way forward to remediate water pollution

Divya Yadav,[a] Karmjeet Nain,[a] Divya Dhillayan,[a] Rishi Mittal,[a] Shafila Bansal[b] and Santosh Bhukal *[a]

Received 12th September 2023
Accepted 10th January 2024

DOI: 10.1039/d3va00269a

rsc.li/esadvances

In this investigation, bare and hydrophobic IL-modified FeO nanoparticles (NPs) have been synthesized using microwave irradiation. Multiple characterization techniques, including XRD, FT-IR, and FESEM, were utilized to analyze the properties of the synthesized NPs. The primary objective was to examine the efficacy of NPs as adsorbents for removing dyes and heavy metals from aqueous solutions. To evaluate the factors affecting the adsorption efficiency of the NPs, various variables including dye concentration, pH of the reaction medium, nanoparticle dosage, and reaction time were studied using the batch experiment method. The study demonstrated that the IL-modified NPs were more effective in removing CV and Cr(VI) dyes than unmodified NPs. Various adsorption isotherm intra-particle diffusion models, including Langmuir, Freundlich, and Tempkin, were elaborated to obtain insight into the adsorption behavior of the NPs. This study effectively synthesized bare and IL-modified NPs using a microwave irradiation method. The modified NPs showed promising potential as adsorbents for efficiently removing CV dye and Cr(VI) from aqueous solutions.

Environmental significance

Nanotechnology and room temperature ionic liquids (RTILs) are powerful tools in water remediation. They offer a more sustainable and environmentally conscious solution to water pollution and scarcity. Traditional methods often rely on chemical agents, which can have negative environmental and health impacts. By combining nanotechnology with RTILs, the reliance on chemicals is minimized, resulting in a reduced environmental footprint. Nanomaterials can be used to selectively adsorb, degrade, or immobilize waterborne contaminants, replacing the need for large quantities of chemicals. RTILs, with their thermal stability and non-volatile nature, are safer alternatives to volatile and flammable organic solvents. Their properties can be customized by selecting specific combinations of cations and anions, making them versatile solvents for diverse applications. Ionic liquids (ILs), which include RTILs, can modify nanoparticles (NPs) to remove contaminants like CV dye and chromium from water. This synergy between ILs and nanotechnology extends the toolbox of innovative solutions for addressing water pollution issues. Overall, the integration of nanotechnology and RTILs is a promising approach to revolutionize water remediation, reducing chemical usage and maximizing efficiency through tailored materials and processes.

1. Introduction

Industrial effluents discharged into water bodies pose a significant concern, restricting human progress and hindering environmental sustainability.[1] In the context of India, the dye industry holds a strong position, accounting for a significant share of the global market, and is projected to grow further in the coming years. The industry's growth is driven by rising disposable incomes, population expansion, increased demand for cosmetic products, construction, infrastructure development, and paints and coatings.[2] The production of pigments and dyes, particularly in industries such as cosmetics, textiles, paper, and leather, poses a significant environmental threat by contributing to water contamination and diminishing the availability of safe drinking water.[3,4] The poor biodegradability of organic dyes, often with carcinogenic properties, exacerbates the risks of water pollution. Some dyes contain toxins, and their breakdown products can be more hazardous than the original pigments. Toxicity experiments reveal that these breakdown products can be extremely harmful to aquatic creatures, surpassing the toxicity of the parent dyes.[5] Moreover, synthetic dyes are often combined with heavy metals like copper, chromium (Cr(VI)), and nickel to enhance colorfastness and brightness. However, the destruction of these dyes during wastewater treatment releases heavy metals into the environment, further polluting water bodies and posing threats to ecosystems and human health.[6–8] Water-soluble dyes, particularly cationic dyes used in textiles, exhibit water solubility and generate positively

[a]*Guru Jambheswar University of Science & Technology, Hisar, 125001, India. E-mail: santoshesegju@gmail.com; divyarao096@gmail.com; karmjeetsinghnain@gmail.com; divyadhillayan@gmail.com; rishimittal.cool@gmail.com; shafibansal@yahoo.co.in*

[b]*Sabudh Foundation, Mohali, 140307, India*

charged ions, producing colored cations when dissolved. Despite their vibrant colors, these dyes raise concerns due to their toxicity. Examples include methane dyes, anthraquinone dyes, cationic azo dyes, phthalocyanine dyes, and others. On the other hand, anionic dyes, relying on negatively charged ions, encompass various compounds, including reactive dyes that may be released into the environment undesirably. Acidic silks, used in dyeing various fibers, are of concern due to their organic sulphonic acids, potentially harmful to human health.[9–14] Heavy metal pollution, resulting from activities such as electroplating, pesticide production, battery manufacturing, tanning, mining, and metal smelting, has become a matter of growing concern, causing environmental degradation and harm to human health.[15–17] Specific pollutants like crystal violet and hexavalent chromium are particularly problematic. Crystal violet is carcinogenic and recalcitrant, persisting in various environments.[18] Hexavalent chromium is a highly toxic heavy metal commonly released by industries, posing threats to ecosystems and human well-being. The US Environmental Protection Agency considers it the highest-priority toxic pollutant.[19] Chromium, especially in its hexavalent state, is a more toxic heavy metal than others released from various industries. The Indian standard for drinking water (ISO:10500) sets an acceptable limit of 0.05 mg L^{-1} for chromium.[20] In recent years, low-cost materials such as nanoparticles with high surface area and good thermal stability, including iron oxide, zinc oxide, aluminum oxide, titanium oxide, mixed oxide, gold nanoparticles, and copper oxide, have been utilized for adsorption to remove pollutants.[21,22]

Various techniques have been employed to address this issue, including ion exchange, flocculation, reverse osmosis, co-precipitation, ultrafiltration, oxidation, and solvent extraction. However, the adsorption technique stands out due to its cost-effectiveness and minimal sludge production. Activated charcoal has been widely studied and proven effective as an adsorbent for wastewater treatment.[23–27] However, its high cost and regeneration challenges limit its widespread use.

In environmental remediation, nanotechnology plays a significant role, particularly in processes such as effluent treatment, potable water purification, groundwater remediation, and air purification.[28] Metal NPs exhibit catalytic properties that are highly beneficial in organic reactions due to their ease of preparation and high recovery rates. Metals such as palladium and copper have been extensively utilized as catalysts in the synthesis of various compounds. Metal NPs also show potential as photocatalysts for environmental remediation and require further research.[29]

Certain metal NPs have demonstrated strong adsorption capacities and are utilized in environmental remediation processes. Examples of such NPs include TiO_2,[30] ZnO,[31] and Ag NPs.[32] Iron (Fe) NPs, in particular, offer several advantages over other types of metal NPs. They are less toxic to organisms and relatively more cost-effective.[33]

Iron NPs are among those NPs that possess significant redox and adsorption capacities, making them valuable in diverse sectors, including medical treatment, sensing, catalytic activity, optics, electronic devices, and environmental remediation.[34] However unmodified FeO NPs tend to aggregate into bigger particles in solutions. Room-temperature ionic liquids (RTILs), which are made up of just cations and anions, are used for stabilising NPs without the need for extra organic chemicals.[35]

Due to the fact that their cations and anions may be tuned to meet the needs of a specific application, ILs are sometimes referred to as designer solvents. Therefore, these green solvents can be hydrophilic or hydrophobic depending on the makeup of cations and anions. The main reason for using ILs in the reaction system of nanoparticle synthesis is to control the rate of particle growth and nucleation, which is important for predicting the size and form of the NPs. Long-chain surfactants reduce the rate of particle aggregation, and the pre-organized solvent structure facilitates the creation of highly defined nanostructures by allowing the nanocrystals to self-organize. Anions and large cations in ILs have peculiar properties that make them operate as self-assembling templates.[36,37]

It is essential to adopt sustainable practices and develop effective wastewater treatment methods to tackle the challenges posed by industrial effluents and pollution. The goal is to minimize the release of pollutants into water bodies and ensure the availability of clean water for various purposes. The understanding of dye and heavy metal properties, their behavior during treatment processes, and the development of advanced treatment technologies are crucial for mitigating the environmental impact of the pollutants. Through continuous research and innovation, we can work towards sustainable and responsible production practices that minimize water pollution and safeguard both the environment and human well-being.

The present study involved the synthesis of bare and IL-functionalized FeO NPs through the application of microwave irradiation methodology. Hydrophobic IL based NPs were synthesized using 1-butyl-3-methylimidazolium hexafluorophosphate (IL-1) and 1-ethyl-3-methylimidazolium bis(trifluoromethylsulfonyl) imide (IL-2). The synthesized NPs were subjected to experimental conditions to eliminate potentially dangerous crystal violet (CV) dye and Cr(VI) heavy metal. This work is novel because hydrophobic ionic liquids 1-butyl-3-methylimidazolium hexafluorophosphate (IL-1) and 1-ethyl-3-methylimidazolium bis(trifluoromethylsulfonyl) imide (IL-2) have not been used before for modification of iron nanoparticles and their use for removal of CV dye and Cr(VI) has not been reported before. The study endeavors to examine the influence of surface modification by comparing the adsorption efficacy of bare and IL-modified NPs.

2. Methodology

2.1 Materials

The chemicals used in this investigation were of standard scientific quality and in their pure form without any alteration. Sodium hydroxide in powder form (minimum assay = 97.0%), ferrous sulphate heptahydrate AR and ferric chloride SRL (minimum assay = 99% and 98% respectively), 1-butyl-3-methylimidazolium hexafluorophosphate and 1-ethyl-3-methylimidazolium bis(trifluoromethyl sulfonyl) imide (minimum assay HPLC/total nitrogen = 98.0%), ethanol (purity

≥ 99.9%), crystal violet and potassium dichromate ($K_2Cr_2O_7$) were purchased from Central Drug House (CDH), New Delhi. Double distilled water was used for all experiments. The pH of the solutions was changed by adding (1.0 M) NaOH and (0.1 M) HCl.

2.2 Synthesis of iron oxide (FeO) NPs (bare and IL-modified)

The microwave irradiation approach was used to synthesize all three NPs (bare FeO NPs, IL-1 modified and IL-2 modified NPs). 2 M ferric chloride and 1 M ferric sulphate were prepared and 200 mL of each were taken and mixed to prepare solution-A and vigorously stirred on a magnetic stirrer. 1.0 M NaOH was simultaneously added dropwise until the pH of the mixture reached 11. The resultant mixture was then placed in an IFB-25SC4 microwave oven with an output power of 850 W for 10 minutes while being kept still to allow the precipitate to develop. After centrifuging the solution, the precipitate was carefully cleaned with distilled water and ethanol. The precipitate was cleaned and then left to dry at 60 degrees Celsius in a hot air oven for 10–12 hours. At the end of the reaction, bare FeO (unmodified) NPs were synthesized.[33] In order to synthesize the necessary modified NPs for FeO, 50 ml of a 0.2 M solution of ILs was added to solution-A before adjusting the pH by the aforementioned method.[38]

2.3 Characterization of the synthesized NPs

Various techniques were utilized to inspect the optical, structural, compositional and morphological properties of the prepared NPs. The morphological properties of the synthesized NPs were studied using a Field Emission Scanning Electron Microscope (FESEM) with EDX. The NPs' surface morphology was analyzed by collecting images at magnification 50 000× with a JEOL FE-SEM (Semtrac, Japan). A Fourier Transform Infrared (FT-IR) spectrometer (PerkinElmer), with a specific spectral range of 500 to 4000 cm^{-1}, resolution power of 0.5 cm^{-1} and based on the way it interacts with infrared light, potassium bromide powder, which provides a conventional optical method for data collection, was used to identify and analyze the chemical composition of the materials. The particle size and crystalline constitution of the synthesized NPs were analysed using an XRD instrument (BENCHTOP MINI FLEX-II, RIGAKU, JAPAN) in the range of 10°–80° with $\lambda = 0.154$ nm. The Debye–Scherrer equation was used to calculate the size of the NPs:[39]

$$d = 0.9\lambda/\beta \cos\theta \quad (1)$$

where d is the diameter of the crystalline size of the NPs, 0.9 is the shape factor constant, λ is the X-ray wavelength (0.154 nm), θ is Bragg's angle in radians, and β is the full width at half maximum intensity of the peak (FWHM). Additionally, Transmission Electron Microscopy (TEM, Hitachi H-7100) was employed to verify the presence of pure elemental iron oxide nanoparticles. Zeta potential measurements were conducted on a 10% aqueous suspension using a Malvern Instruments Ltd Zetasizer Nano ZS. Before zeta potential measurements, all samples were sonicated for 5 minutes. To measure the surface area and porosity of the prepared nanomaterials BET analysis was carried out.

2.4 Batch mode study

In the conducted adsorption experiments, a systematic exploration of various parameters was undertaken to unravel the intricate dynamics of the process. The investigations for CV dye removal involved varying the dye concentration (ranging from 10 to 60 ppm), adjusting the amount of nanoparticles (from 0.005 to 0.03 g), tuning the operating pH levels (ranging from 2 to 12), and assessing the reaction duration (from 10 to 120 minutes) utilizing an orbital shaker at room temperature. Similarly, these experiments aimed to comprehensively explain the adsorption of Cr(VI) by the adsorbent under diverse conditions. The study involved a detailed examination of the adsorbate concentration across a range from 10 mg to 250 mg and ion concentrations varying from 20 ppm to 160 ppm. The impact of contact time on the adsorption process was scrutinized meticulously, covering durations from 20 to 120 minutes. Furthermore, the pivotal role of pH in adsorption phenomena was highlighted, with the experimental focus specifically ranging from pH 2 to 12. This extensive spectrum of experimental conditions collectively contributes to a thorough comprehension of the factors influencing the adsorption of Cr(VI) by the adsorbent, offering valuable insights for optimizing and enhancing the efficiency of the process across diverse scenarios. The content of Cr(VI) was analysed using a UV-visible spectrophotometer (Model UV-1800 Shimadzu). The pH value of the solution was adjusted by adding 0.1 mol L^{-1} concentrations of HCl and NaOH. The settings of the experiment were optimised for a concentration of 30 ppm dye and a pH of 10.0 during a period spanning from 20 to 120 minutes for the kinetics of adsorption. Subsequently, samples were extracted, centrifuged at 3000 rpm for 5 minutes, and filtered with Whatman filter paper no. 1. A UV-Vis spectrophotometer was utilized to find out the residual CV amount after treatment.

The following equation was used to calculate the adsorption efficiency of the synthesized NPs for both CV dye and Cr(VI):[40]

$$\text{Adsorption efficiency } (\%) = \frac{C_i - C_f}{C_i} \times 100\% \quad (2)$$

where C_e represents the residual dye concentration (mg L^{-1}) and C_i stands for the initial dye concentration (mg L^{-1}). The dye concentration values for all the samples prior to and post adsorption were obtained using the equation shown below to calculate the amount of dye adsorbed:[41]

$$q_e = (C_i - C_e) \times \frac{V}{m} \quad (3)$$

where m denotes the mass of adsorbent (g), q_e (mg g^{-1}) denotes the amount of CV dye adsorbed by the NPs at equilibrium, and V stands for the volume of the solution (L).

3. Results and discussion

3.1 Characterization and properties of FeO NPs

3.1.1 Fourier transform infrared spectroscopy (FT-IR) analysis. FTIR spectroscopy was used to confirm the chemical compositions of the iron oxide NPs at room temperature. Fig. 1 displays the three FTIR spectra of modified and unmodified

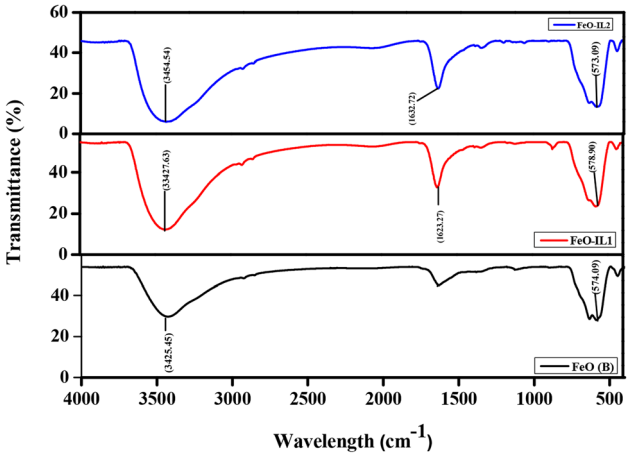

Fig. 1 FTIR spectra of the synthesized bare FeO NPs and modified NPs with IL-1 and IL-2 under identical reaction conditions.

NPs. The presence of the iron–oxygen bond (Fe–O) in the synthesised NPs is confirmed by the appearance of distinct peaks at 574.09, 578.90, and 573.09 cm^{-1} for FeO (B), FeO-IL1, and FeO-IL2 connected to the resonance of Fe–O octagonal bonds.[42] In addition, the observed peaks at 1623.27 and 1632.72 cm^{-1} are only clearly visible in the product synthesized using an ionic liquid as these peaks show skeleton vibrations of the imidazole ring. The peaks at 3435.45, 3427.63, and 3454.54 cm^{-1} for FeO(B), FeO-IL1, and FeO-IL2 respectively show the vibrational bending of absorbed water and OH stretching mode. Because water is utilised as a sample solvent, the surface hydroxyl ion is stretched, causing the OH group of water to stretch. The experimental findings demonstrate that the NPs synthesised are made of iron oxide and do not include any significant contaminant.[43]

3.1.2 XRD analysis. The table provided in Fig. 2 contain comprehensive information regarding the peaks and corresponding sizes of the synthesized NPs. The distinct peaks as shown in Fig. 2 are within the range of 10°–80° across all compositions indicative of the crystalline nature of the compound. Using Scherrer's formula, it is calculated that the NPs were of 11.58 nm, 8.22 nm and 6.97 nm for bare FeO, FeO-IL1, and FeO-IL2 respectively.[44] The ILs can control crystal growth during the growth of NPs as size reduction is observed because of three most likely reasons that are (a) interactions between the rings of aromatic compound structures, (b) hydrogen bonding between the initial nuclei and the hydrogen atom, and (c) steric crowding in the imidazolium ring system generated by the extended length of the ILs' alkyl chains depending on the nitrogen.[45] The orthorhombic shape structure of iron oxide (JCPDS card no. 19-1346) indexed in the diffractograms show 2 peak values as described in Fig. 2(b).[46]

3.1.3 Field emission scanning electron microscope (FE-SEM) analysis and energy dispersive X-ray analysis (EDAX). The FE-SEM pictures (with various resolutions) of bare and IL-modified FeO NPs demonstrate an even spread of NPs of various forms (Fig. 3). The size of bare NPs ranged from 5 nm to 12 nm. However, with IL-modified NPs, extremely small particles have been obtained. Table 1 displays the amount (%) of iron metal and oxygen in the synthesized NPs (Fig. 4).[47]

3.1.4 Brunauer–Emmett–Teller (BET). The surface area was calculated using BJH adsorption/desorption isotherms obtained in liquid nitrogen (77.35 K) as shown in Fig. 5. The specific surface area of the nanomaterials is obtained from BET, while the total surface area of the pores obtained from the BJH desorption analysis along with the pore diameter is shown in Table 2.

3.1.5 Zeta potential measurements. The solution samples of FeO-bare, FeO-IL1 and FeO-IL2 NPs were prepared in double distilled water (DDW) and their zeta potentials were measured to be −1.96, −17.1, and −11.6 respectively as shown in Fig. 6. The shift in zeta potential towards negative values in contrast to unmodified synthesis demonstrates that ILs considerably affect the interfacial structure of NPs, reducing the NP aggregation ability.[48]

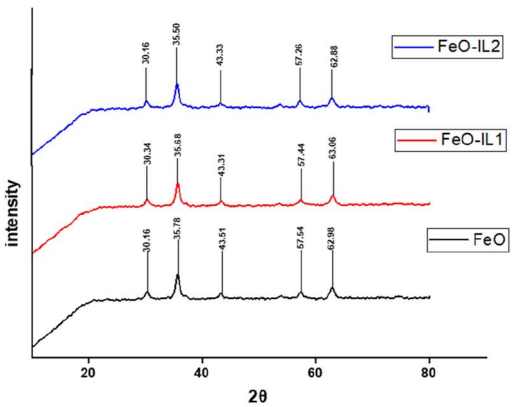

Peaks	Bare	IL-1	IL-2
Fe	30.32 °	30.32 °	30.26 °
	35.64 °	35.70 °	36.58 °
	43.32 °	43.38 °	43.34 °
	57.41 °	57.44 °	57.20°
	62.92 °	62.96 °	63.20 °

(b)

Fig. 2 (a) XRD patterns of the as-prepared iron oxide nanoparticles using IL-l and 2 and without IL under similar reaction conditions; (b) table listing the peaks shown in the XRD patterns.

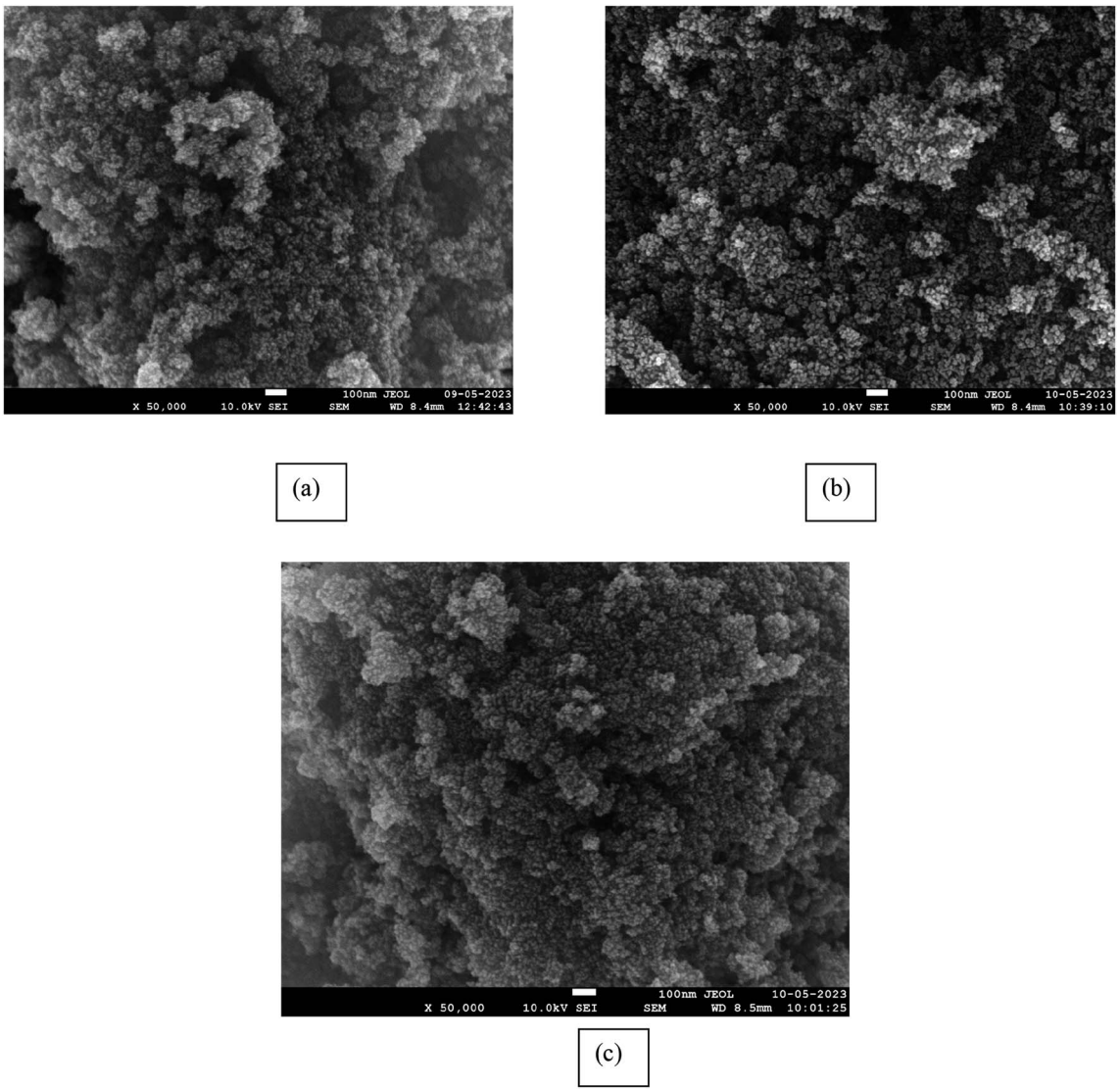

Fig. 3 SEM images of the as-prepared (a) bare FeO NPs and (b) IL-1 modified and (c) IL-2 modified NPs under similar reaction conditions.

3.1.6 TEM. Fig. 7 presents the high-resolution transmission electron micrographs of both bare and modified NPs. The TEM images depict the diverse spherical shapes of nanoparticles and their consistent encapsulation within ionic liquids. The micrograph distinctly illustrates a decrease in size and aggregation of modified NPs compared to the bare FeO NPs. Furthermore, IL-1 modified FeO NPs exhibit surfaces characterized by increased roughness, featuring mesoporous structures and fewer particle aggregates compared to both bare and IL2 modified NPs.

3.2 Results and discussion of the adsorption reaction of CV dye

3.2.1 The effect of pH on the adsorption of CV dye. The pH of the solution is critical in the adsorption process of dyes utilising NPs since both the adsorbent and the adsorbate may possess groups with functional properties that might be affected by the presence of hydrogen ions. To assess the impact of pH on the adsorption efficiency of FeO NPs, this study conducted experiments with varying pH levels ranging from 2 to 12. The NPs used in the study were either in their naked form or modified with ILs, and the dosage of NPs remained constant at 30 mg/30 mL, while the initial dye concentration was set at 30 ppm.

The results depicted in Fig. 8(a) demonstrated that, initially, an increase in the pH of the solution led to a gradual enhancement in the rate of dye adsorption for all cases. At pH 10, the dye breakdown rate was maximum. However, as the pH further increased, there was a subsequent decline in the rate of adsorption. Furthermore, the IL-modified NPs exhibited the highest adsorption capacity compared to the unmodified NPs.

These findings highlight the pH-dependent nature of the dye adsorption process using FeO NPs. The increased adsorption rate at higher pH values up to pH 10 can be attributed to favorable electrostatic interactions between the charged functional groups on the NPs and the dye molecules. However,

Table 1 The amount (%) of metal and oxygen in the synthesized NPs

Element	Weight %	Atomic %	Error %	*R*	*A*	*F*
Fe bare						
O K	46.9	75.5	9.0	0.8683	0.2302	1.0000
Fe K	53.1	24.5	2.2	0.9433	0.9720	1.0292
Fe PF6						
O K	36.0	66.3	9.3	0.8538	0.2110	1.0000
Fe K	64.0	33.7	2.2	0.9344	0.9689	1.0275
Fe IMIDE						
O K	45.7	55.1	10.0	0.8975	0.1273	1.0000
Fe K	54.3	11.6	2.1	0.9597	0.9795	1.0344

beyond pH 10, the decrease in adsorption rate may be due to changes in the surface charge characteristics of the NPs or the dye, leading to reduced affinity between them. Additionally, the enhanced adsorption efficiency of the IL-modified NPs suggests that the presence of ILs on the NP surface enhances the interactions with the dye molecules, leading to improved adsorption performance.[49,50]

3.2.2 Effect of the adsorbent dose of CV dye. For 60 minutes, we did batch adsorption experiments with NP dosages that varied from 10 to 50 mg in 30 mL at a starting dye amount of 30 ppm and pH of 10. All experiments were carried out in an orbital shaker at room temperature. Adsorption efficiency increased with NP dose in both unmodified and IL-modified NPs, but above a specific dose (>20 mg), the % clearance efficacy held steady, as shown in Fig. 8(b). For both IL-1 and 2 modified FeO NPs, the maximum efficiency of adsorption is greater than 95%. Despite the quantity of NPs being greater than 30 mg, their adsorption ability stayed static because, at greater quantities, the aggregation speed of NPs increased, reducing the total surface area of NPs and restricting adsorption effectiveness.[51]

3.2.3 Effect of CV dye concentration. The influence of the concentration of dye on the adsorption capability of FeO NPs was investigated by adjusting the concentration to 20 ppm–120 ppm at room temperature while retaining the other factors (at which the greatest adsorption was achieved): a pH value of 10 along with the dosage of adsorbent 30 mg/30 mL of sample. In all cases, adsorption effectiveness reduces significantly with increasing dye concentrations, with IL-modified NPs demonstrating the greatest removal [Fig. 8(c)]. Because the active sites of NPs have been filled with the molecules of dye, increasing the amount of dye had no beneficial effect on dye adsorption efficiency.[52]

3.2.4 Effect of time on the adsorption of CV dye. In an orbital shaker, the impact of time period on the adsorption of

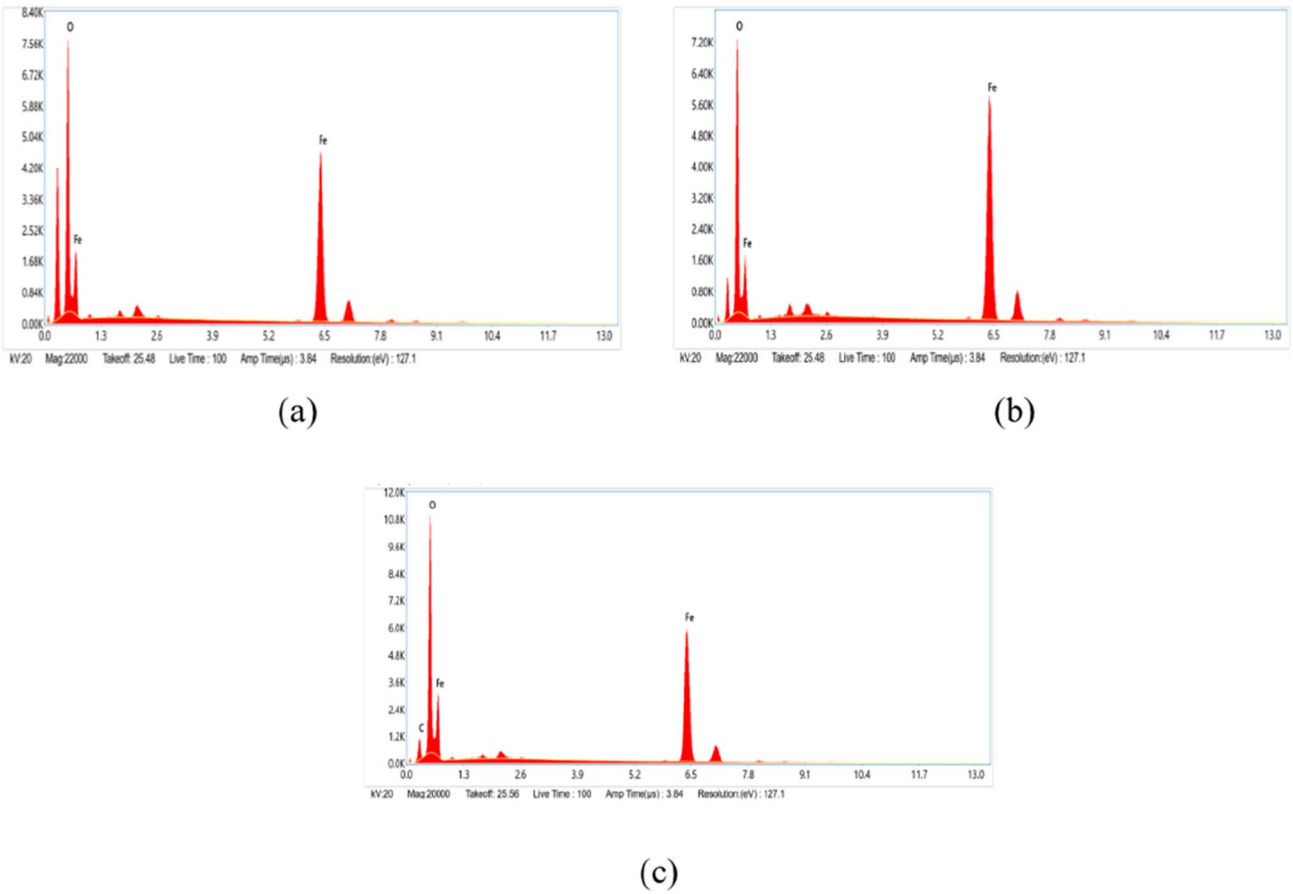

Fig. 4 Typical EDS spectra of the as-prepared FeO NPs using IL-1 (b) and 2 (c) and without IL (a) under similar reaction conditions.

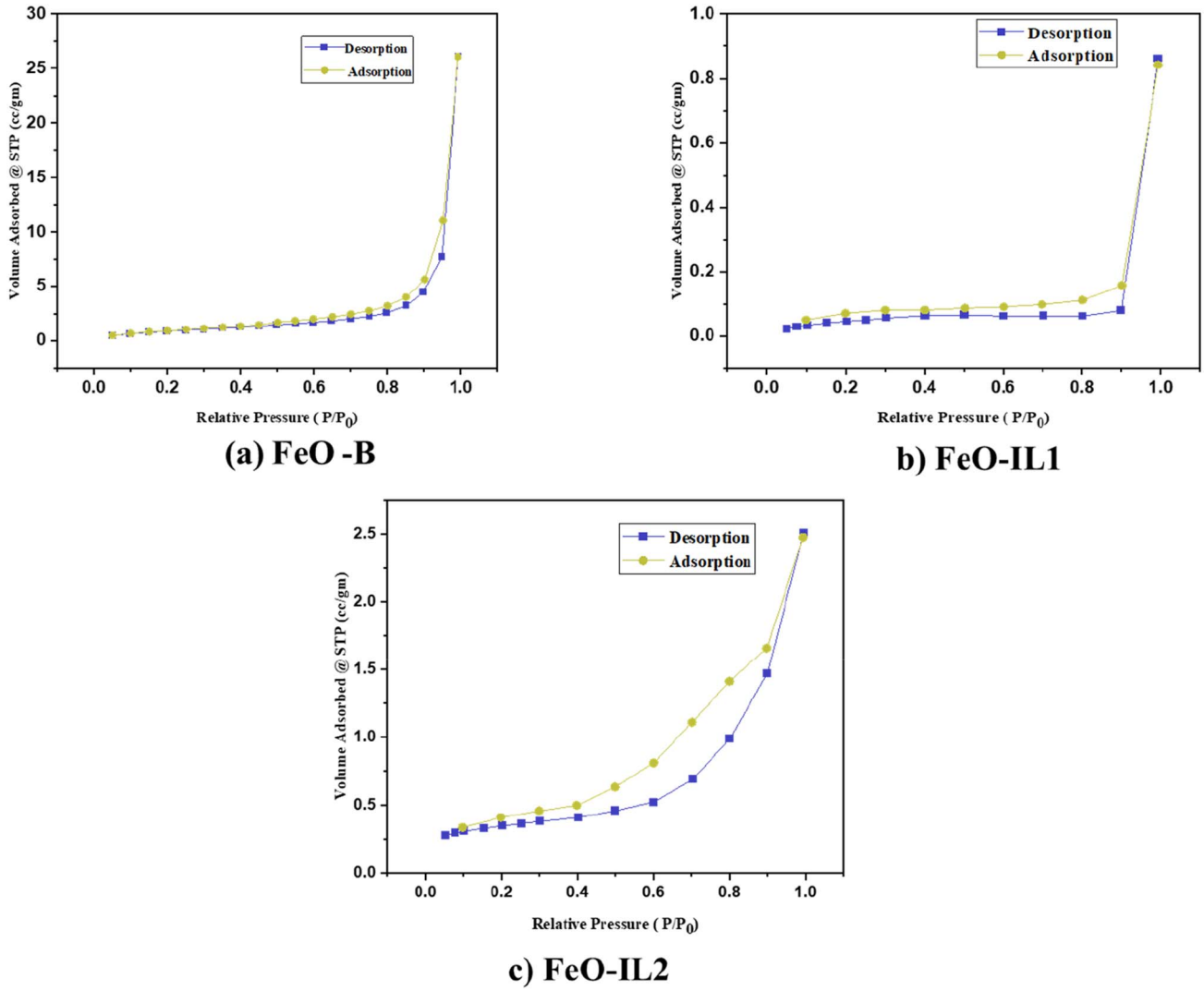

Fig. 5 BJH adsorption/desorption isotherm graphs of (a) FeO-B, (b) FeO-IL1 and (c) FeO-IL2.

Table 2 BET parameters analysis for synthesized NPs

Parameters	Bare FeO	FeO-IL1	FeO-IL2
BET surface area	32.714 $m^2 g^{-1}$	48.256 $m^2 g^{-1}$	45.921 $m^2 g^{-1}$
Pore surface area	46.235 $m^2 g^{-1}$	61.272 $m^2 g^{-1}$	57.852 $m^2 g^{-1}$
Average pore diameter	2.412 nm	4.128 nm	3.578 nm
Pore volume	0.083 cc g^{-1}	0.114 cc g^{-1}	0.102 cc g^{-1}

CV dye by NPs was examined between 10 and 120 minutes at room temperature. In every scenario, the adsorption efficacy increased extremely quickly during the first 10 minutes, then increased progressively for the next 60 minutes and for an additional 120 minutes until the system became saturated as shown in Fig. 8(d). However, IL-modified NPs exhibited the highest eradication efficacy. The effect of duration on removal efficacy can be described by the accessibility of more unoccupied spots on the surface of NPs for the CV adsorption, which become overwhelmed after a certain period of time and as a result no additional adsorption was found with the passage of time.[53]

3.3 Chromium [Cr(VI)] removal

3.3.1 Effect of adsorbent dose. To check the effect of concentration of iron NPs on the adsorption of Cr(VI), some studies were carried out with concentrations ranging from 10 mg to 250 mg with an interval of 40 mg under optimum conditions with the initial concentration of Cr(VI) being 40 ppm and constant pH = 6 for 100 min. The experiments were carried in an orbital shaker with a temperature of 60 °C. The highest adsorption capacity was observed at 170 mg (Fig. 9). Similar findings were reported when FeOs and palladium NPs synthesized using Spirulina were used for adsorption of CV dye and lead respectively.[54]

3.3.2 Effect of Cr(VI) ion concentration. Keeping the other parameters constant, the effect of concentration of Cr(VI) was investigated by varying the ion concentration from 20 ppm to 160 ppm. The pH and the adsorbent dose were kept constant at

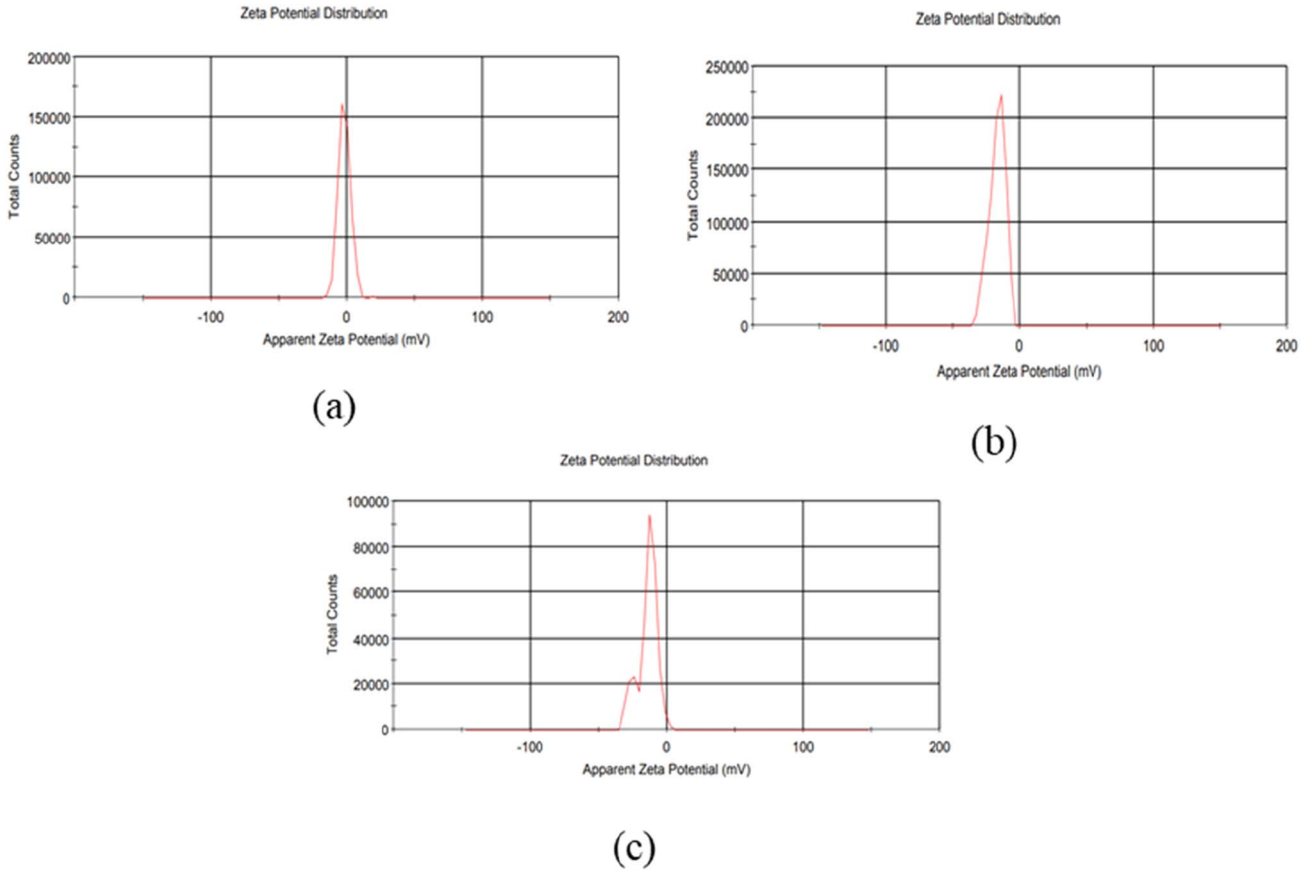

Fig. 6 Zeta potential of (a) FeO-bare, (b) FeO-IL1 and (c) FeO-IL2.

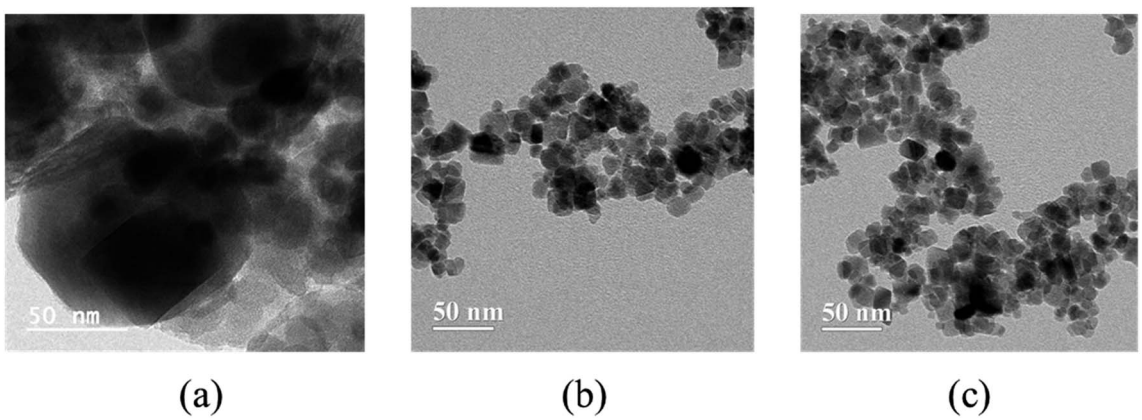

Fig. 7 High resolution transmission electron micrographs of (a) FeO-bare, (b) FeO-IL1 and (c) FeO-IL2.

6 and 170 mg. The solutions were investigated in an orbital shaker with a temperature of 60 °C. The highest adsorption capacity was observed at 40 ppm (Fig. 9). This clearly indicates that adsorption efficiency depends on metal concentration. With an increase in metal concentration, there are more metal ions to bind on adsorption sites, but these sites are limited in number.[55]

3.3.3 Effect of time on the adsorption of Cr(VI). The effect of contact time on the adsorption of Cr(VI) by the adsorbent was examined in the range of 20 to 120 min with an interval of 20 min at 60 °C temperature in an orbital shaker with pH and the adsorbent dose being kept constant at 6 and 170 mg (Fig. 9). The Cr(VI) concentration was 40 ppm. Adsorption efficiency increased as contact time increased from 20 min to 100 min, and at 100 min maximum adsorption was observed.

3.3.4 Influence of pH on adsorption. pH is regarded as one of the significant factors that affects the process of adsorption. pH in this experimental study was varied from 2 to 12, to explore

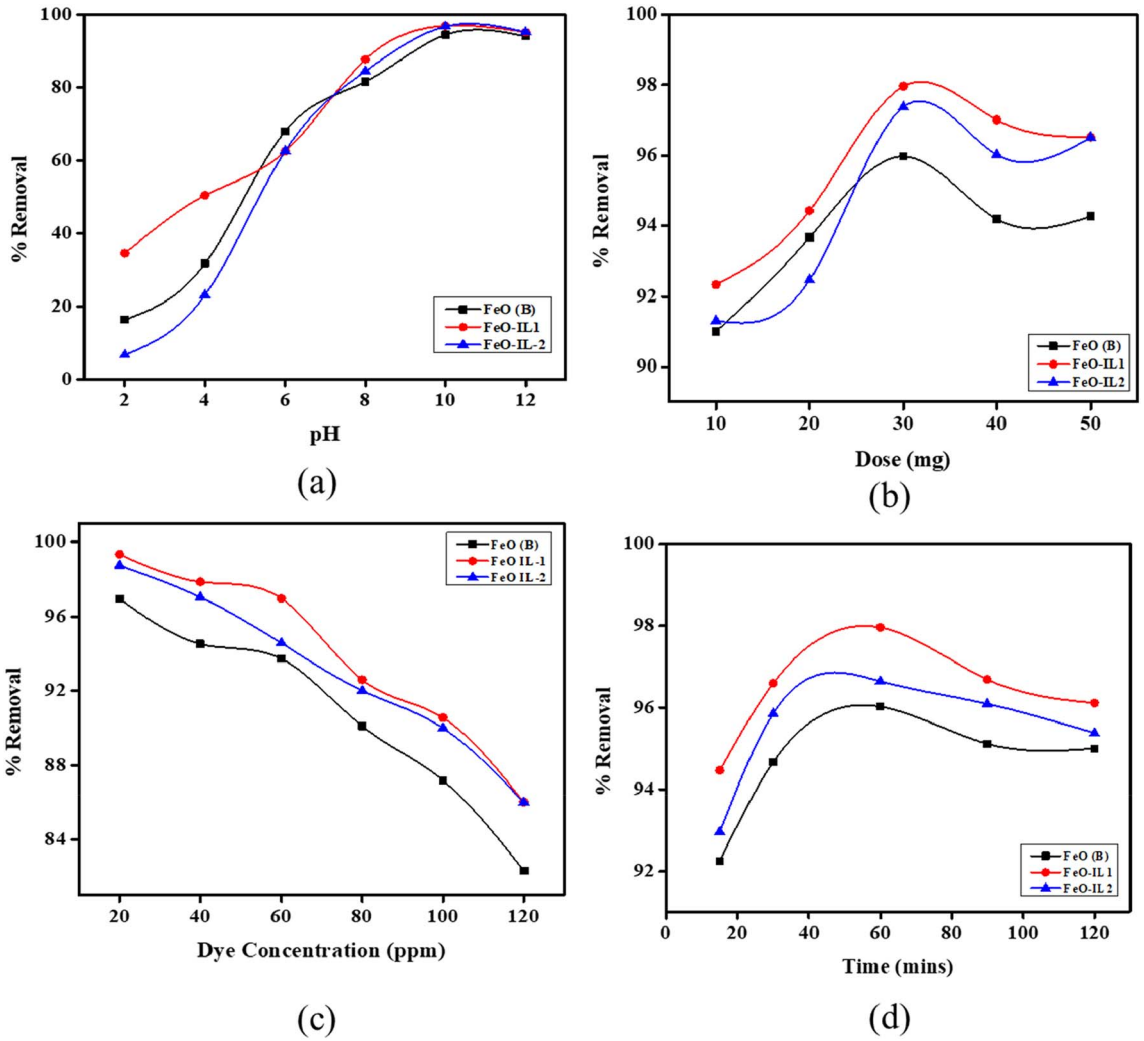

Fig. 8 Graphical representation of the effect of various factors: (a) pH, (b) dose, (c) dye concentration, and (d) time period on the % removal of CV dye using the prepared FeO NPs using IL-1 and 2.

its influence on the adsorption of Cr(VI). The experimental study was carried out at a metal concentration of 40 ppm, temperature of 60 °C, contact time of 100 min and NP dose of 170 mg. Maximum adsorption efficiency was observed at pH of 6. Similar findings were observed when iron NPs synthesized using an algal extract were used for adsorption of Cr(VI).[56]

3.4 Comparison study of different ILs and NPs on optimised parameters

Based on the optimized parameters mentioned above, the maximum adsorption capacity was assessed for IL1, IL2, FeO (B), FeO (IL1), and FeO (IL2) in the removal of CV dye. The results demonstrated that FeO-IL1 exhibited the highest removal efficiency, reaching a maximum adsorption of 98.47%. Additionally, FeO (IL1) showed significant adsorption performance, achieving a removal efficiency of 98.43%. These findings are visually represented in the accompanying Fig. 10.

In the referenced study, a new nanocomposite composed of an [EPMpyr][SAL] ionic liquid and iron oxide magnetic nanoparticles (IL/MNP/Zeo) was successfully synthesized and characterized through diverse techniques. This nanocomposite displayed improved binding properties and thermal stability, acting as an effective catalyst for reducing nitroanilines and dyes in aqueous solutions. Notably, the catalyst, easily recoverable *via* an external magnet, demonstrated outstanding recyclability with minimal loss of activity, highlighting its promising potential for environmentally friendly and cost-effective applications in environmental protection.[57] A comparison between different NPs and ILs at a constant pH of 6, contact time of 100 min, metal concentration of 40 ppm, NP dose of 170 mg and temperature of 60 °C was made. Maximum Cr(VI) metal removal was observed with FeO-IL2 with a maximum adsorption of 77.21% as shown in Fig. 11. Numerous studies have demonstrated the efficacy of both natural and modified adsorbents in eliminating heavy metal pollutants, attributing their adsorption capabilities to their expansive surface area and pore volume.[58] Agricultural by-products and clay minerals have been effectively employed for

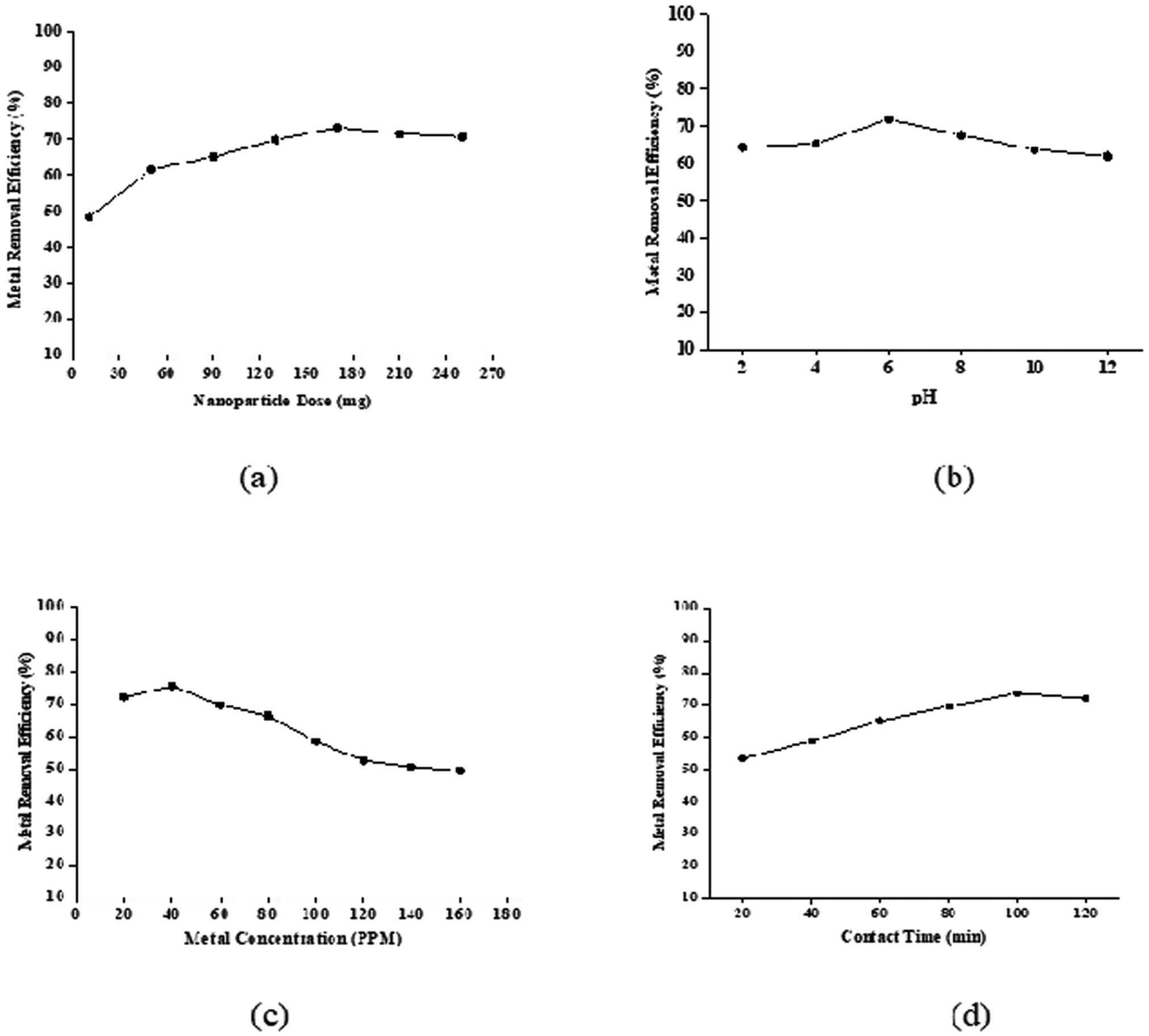

Fig. 9 Graphical representation of the effect of different parameters: (a) dose, (b) pH, (c) metal concentration, and (d) time on the % removal of chromium heavy metal using the prepared bare-FeO NPs.

the removal of heavy metals and inorganic pollutants, as highlighted by Balarak *et al.* (2016a).[59] Notably, Bazrafshan *et al.* (2017)[60] investigated the ability of *Cydonia oblonga* seeds to remove Cr(VI) ions from aqueous solutions. Balarak *et al.* (2016b)[61] provided studies on the removal of cadmium from water by treating *Azolla filiculoides* with sulfuric acid (H_2SO_4), suggesting the efficacy of *Azolla Filiculoides* as an adsorbent for Cd(II). Furthermore, Balarak *et al.* (2016a)[59] revealed that barley husk, a cheap agricultural waste, was effective in removing Cd(II) from aqueous solutions. Azarpira and Mahdavi (2016)[62] studied the utilisation of canola biomass for a batch-based adsorption of Cd(II) from aqueous solutions in another investigation. Agarwal *et al.* (2016)[63] have reported the elimination of hazardous nickel(II) utilising novel alumina nanoparticles and multiwalled carbon nanotubes.

3.5 Different adsorption isotherm models

The isotherm models were used to evaluate adsorption behaviour and interactions between adsorbent and dye molecules. To investigate the adsorption equilibrium of CV dye onto the surface of NPs, the adsorption isotherm models *viz.* Langmuir,[64] Freundlich,[65] and Temkin[66] were applied for the adsorption data. The Langmuir model predicts dye molecules binding in a monolayer with uniform distribution of active sites on the adsorbent's surface.[64] The Freundlich model posits that dye adsorbs in many layers on an adsorbent's heterogeneous active sites and that the amount of dye adsorption rises indefinitely as dye concentration increases.[65] The Temkin isotherm model assumed a homogeneous distribution of binding energy through the process of attraction among the dye molecules and the adsorbent, and the heat of dye adsorption decreased linearly

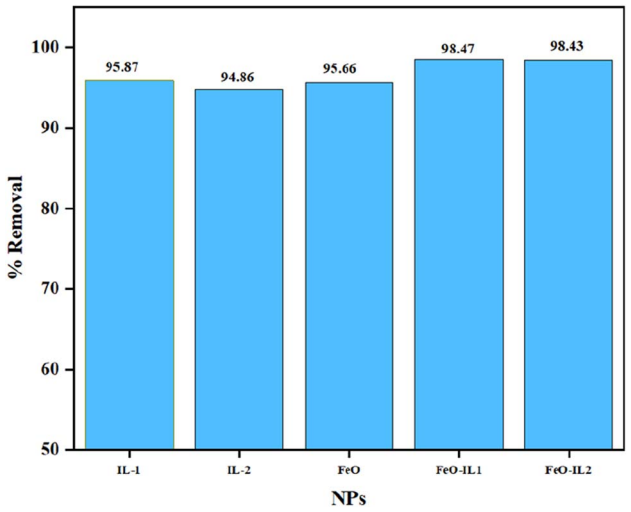

Fig. 10 Graphical representation of comparison of different NPs at optimized parameters.

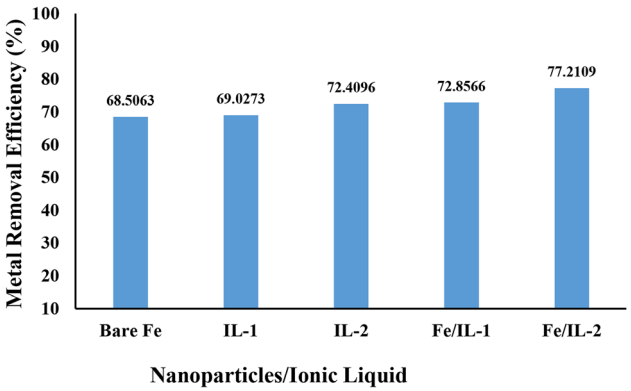

Fig. 11 Graphical representation of the comparison of different NPs at optimized parameters for Cr(VI) removal.

with coverage.[66] Eqn (4)–(6) provide the linear forms of these models *i.e.*, the Langmuir, Freundlich, and Temkin models.

$$\frac{C_e}{q_e} = \frac{1}{q_{max} b} + \frac{C_e}{q_{max}} \quad (4)$$

$$\log q_e = \log K_f + \frac{1}{n} \log C_e \quad (5)$$

$$q_e = B \ln K_T + B \ln C_e \quad (6)$$

where C_e (mg L^{-1}) is the equilibrium concentration of the CV dye solution, and q_{max} (mg g^{-1}) and b (L mg^{-1}) are the maximum adsorption capacity and Langmuir constant, respectively. The amount of dye adsorbed is denoted by q_e (mg g^{-1}). The Freundlich constant is K_F (mg g^{-1}), and the heterogeneity factor is $1/n$. K_T (L g^{-1}) denotes the equilibrium binding constant. The value of $1/n$ should be $0 < 1/n < 1$ for a favorable adsorption process. Cooperative adsorption is indicated by a value of $1/n$ greater than 1, chemisorption by a value of $1/n$ less than 1, and heterogeneous surfaces by a value of $1/n$ near zero. Furthermore, the separation factor (R_L) can be used to explain the major properties of the Langmuir isotherm.

$$R_L = \frac{1}{1 + bC_i} \quad (7)$$

where C_i (mg L^{-1}) denotes the initial concentration of the solution and R_L denotes the separation factor. When $R_L > 1$ the adsorption is unfavorable whereas when R_L has values ranging from 0 to 1 then the nature of adsorption is favorable. $R_L = 1$ suggests linear adsorption.

Table 3 (a) Adsorption isotherm model (Langmuir) parameters for CV dye adsorption onto FeO(B), FeO IL-1, and FeO IL-2 NPs. (b) Adsorption isotherm model (Tempkin) parameters for CV dye adsorption onto FeO(B), FeO IL-1, and FeO IL-2 NPs. (c) Adsorption isotherm model (Freundlich) parameters for CV dye adsorption onto FeO(B), FeO IL-1, and FeO IL-2 NPs

(a) Langmuir

	Parameters	Coef.
FeO(B)	q_{max} (mg g^{-1})	23.94
	b (L mg^{-1})	0.2483
	R_L	0.118
	R^2	0.990
FeO IL-1	q_{max} (mg g^{-1})	58.03
	b (L mg^{-1})	0.639
	R_L	0.049
	R^2	0.992
FeO IL-2	q_{max} (mg g^{-1})	38.25
	b (L mg^{-1})	0.400
	R_L	0.076
	R^2	0.991

(b) Tempkin

	Parameters	Coefficients
FeO(B)	B	19.275
	K_T (L mol^{-1})	3.0879
	R^2	0.991
FeO IL-1	B	14.438
	K_T (L mol^{-1})	18.401
	R^2	0.984
FeO IL-2	B	16.655
	KT (L mol^{-1})	7.576
	R^2	0.980

(c) Freundlich

	Parameters	Coef.
FeO(B)	$1/n$	0.467
	K_F (mg g^{-1})	21.925
	R^2	0.989
FeO IL-1	$1/n$	0.341
	K_F (mg g^{-1})	34.608
	R^2	0.993
FeO IL-2	$1/n$	0.398
	K_F (mg g^{-1})	29.200
	R^2	0.998

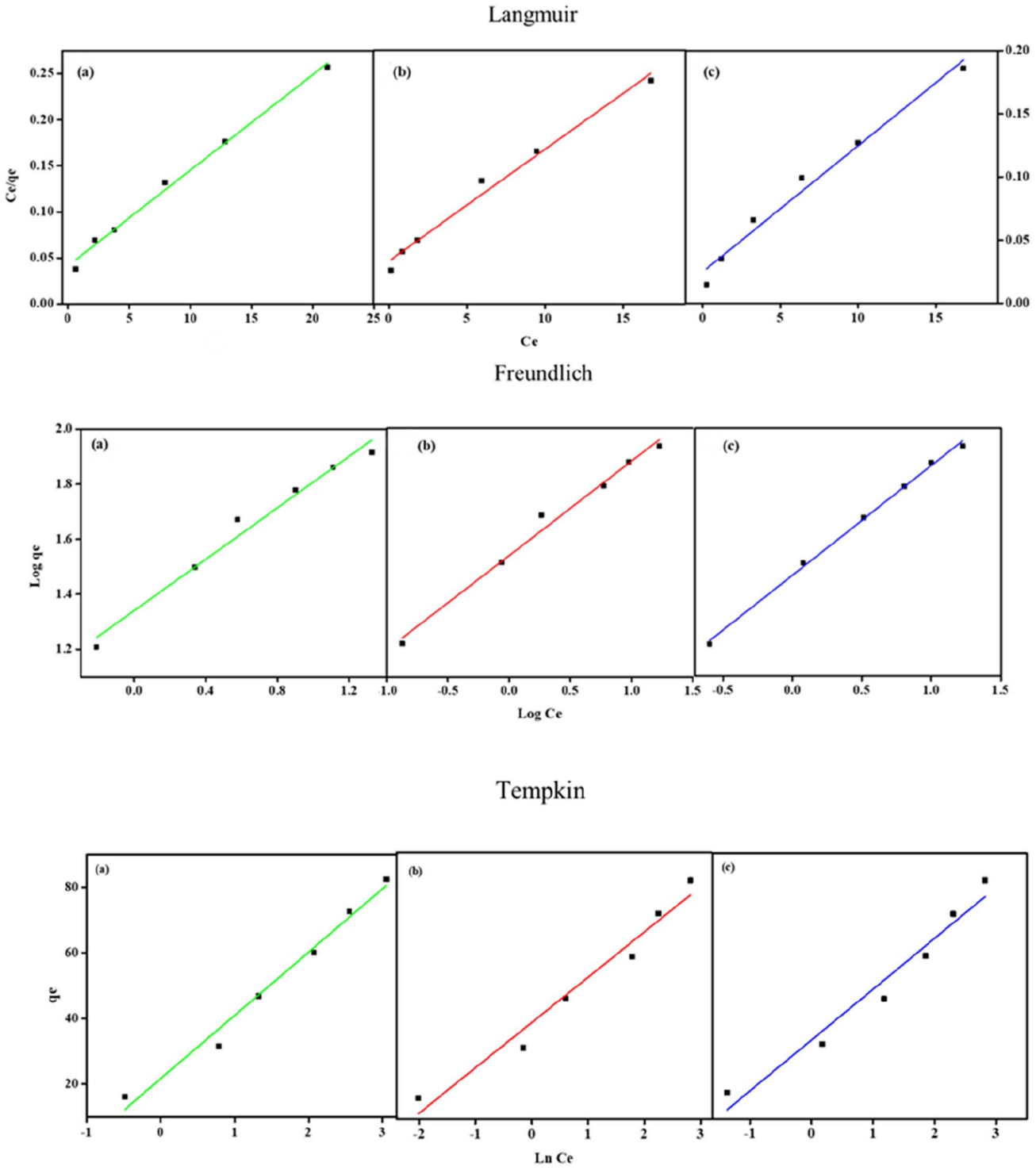

Fig. 12 Langmuir adsorption isotherm, Freundlich adsorption isotherm, and Tempkin adsorption isotherm of CV dye.

The parameters and correlation coefficient (R^2) values in Table 3 were calculated using a linear equation derived from the respective plots of C_e/q_e *versus* C_e, $\log q_e$ *versus* $\log C_e$, and q_e *versus* $\ln C_e$. When the isothermic models' data and parameters were compared, it became clear that Langmuir and Temkin models and experimental data agreed well. Comparing the Langmuir model to the other models under study, its R^2 value of 0.99 indicated a better fit, indicating monolayer adsorption of the CV dye on the surface of NPs and confirming a superior fit of the adsorption process with the Langmuir model (Fig. 12). Standard deviation for all the applied models was presented for CV dye adsorption (Table 8).

3.5.1 Adsorption isotherms for chromium. The parameters and correlation coefficient (R^2) values shown in Table 4 were

Table 4 Adsorption isotherm parameters for chromium

Isotherm models		Bare FeO
Langmuir	q_{max} (mg gm^{-1})	47.664
	K_L (L mg^{-1})	0.025
	R_L	0.442
	R^2	0.965
Freundlich	$1/n$ (L mg^{-1})	0.561
	K_f (mg g^{-1})	2.742
	R^2	0.9289
Temkin	B (kJ mol^{-1})	8.517
	A (L g^{-1})	0.3648
	R^2	0.9867

calculated using a linear equation derived from the respective plots of C_e/q_e *versus* C_e, $\log q_e$ *versus* $\log C_e$ and q_e *versus* $\ln C_e$ (Fig. 13).

When isotherm models' data and parameters were compared, it became clear that the Langmuir model is best compared to Freundlich with its R^2 value of 0.965. Comparing the Langmuir model to the other models under study indicated a better fit. This implies that adsorption happens as monolayers on homogeneous surfaces with little interaction between the adsorbed chromium. A $1/n$ ratio between 0.2 and 0.8 suggests an effective adsorbent, the current experimental investigation showed a $1/n$ value of 0.561, which follows better adsorption. The Q_{max} for the current study obtained using the Langmuir adsorption model was 47.664 mg g^{-1}.

3.5.2 Adsorption kinetics. Designing adsorption procedures and enhancing operating settings to effectively remove pollutants require a kinetics study. As a result, the experimental results for the reaction rate at a solid–liquid interface were examined using "pseudo-second-order" kinetics. Kinetic models in linear form are expressed as eqn (8).

$$\frac{t}{q_t} = \frac{1}{k_2 q_e^2} + \frac{1}{q_e} \quad (8)$$

where q_e (mg g^{-1}) is the amount of CV adsorption at equilibrium time and q_t (mg g^{-1}) is the amount of CV adsorption at contact time t, respectively. The pseudo-2nd-order rate constant

Table 5 Kinetic model of pseudo 2nd order

	Pseudo 2nd order		
Adsorbent	k_2 (min^{-1})	R^2	q_e
Bare	0.007004	0.93	24.05581
IL1	0.010412	0.97	24.41406
IL2	0.042024	0.94	22.07993

is k^2 (g mg^{-1} min^{-1}). A linear plot between t/q_t and t was used to obtain the values of k^2, q_e, and R^2 in the pseudo-second order model. Table 5 shows the derived values of the kinetic model. The regression coefficient (R^2) and model q_e values are crucial parameters for establishing the applicability of each adsorption technique. In accordance to findings, the pseudo 2nd order model has been well adapted to the dye adsorption study. The R^2 value of the pseudo 2nd order model was 0.93, 0.97 and 0.94 for bare, IL1, and IL2 respectively. The q_e value of bare, IL1, and IL2 was 24.05 mg g^{-1}, 24.41 mg g^{-1} and 22.07 mg g^{-1}, respectively which indicates the significance of the pseudo second-order model.[51]

3.5.3 Elovich model. This approach is employed to explain the processes of adsorption that follow second-order kinetics, assuming that the adsorbent's surface is energetically active. It has been widely used in the investigation of chemisorption processes.[64]

The following equation represents the Elovich model equation

$$q_t = 1/\beta \ln(\alpha\beta) + 1/\beta \ln t$$

where q_t = adsorption capacity at time t (mg g^{-1}), α = initial adsorbate adsorption rate (mg g^{-1} min^{-1}) and β = adsorption constant (g mg^{-1}).

A linear plot of q_t *versus* $\ln t$ can be used to determine the initial adsorption rate (α) and adsorption constant (β). This equation is often employed for chemisorption, which is most likely the mechanism that determines adsorption rate. It results in a linear connection with a slope of $1/\beta$ and an

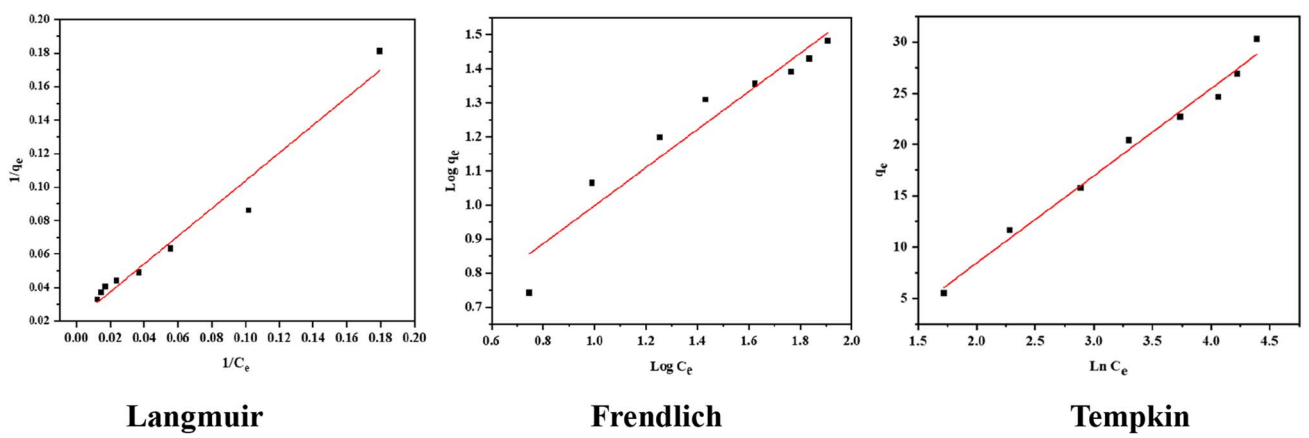

Fig. 13 Langmuir adsorption isotherm, Freundlich adsorption isotherm, and Tempkin adsorption isotherm for Cr(VI) removal.

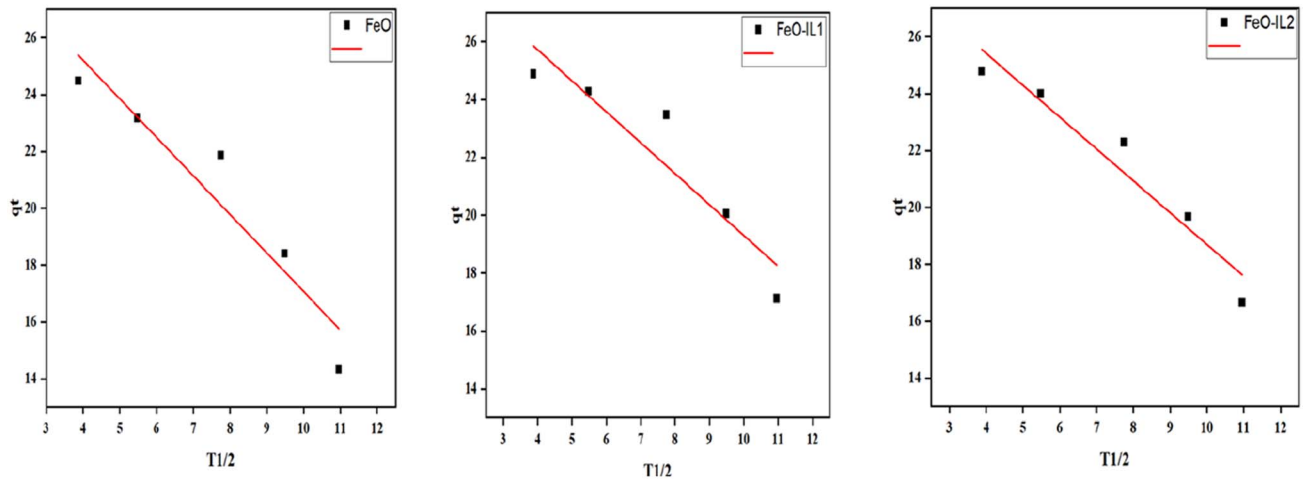

Fig. 14 Intraparticle adsorption models of CV dyes.

intercept of $1/\beta \ln(\alpha\beta)$. The data was collected using the Elovich equation in this study for the adsorption of crystal violet dye from aqueous solution. The low value of the correlation coefficient (R^2) demonstrates that the Elovich model does not fit.

3.5.4 Intraparticle diffusion model. Metal ion molecules may be transported from the bulk into the pores of the adsorbent, as well as adsorption at the adsorbent's outer surface. Adsorption rate-limiting steps can be film diffusion or intraparticle diffusion. Because they act in sequence, the slower of the two will determine the rate (Fig. 14). The ability of metal ion species to diffuse into the interior locations of adsorbent particles was investigated using the Weber–Morris equation.

$$q_t = k_{ipd} t^{1/2} + C$$

The quantity of metal adsorbed 'q' in mg g^{-1} by the adsorbent at time 't' (agitation time in minutes) is represented by the intraparticle diffusion rate constant k_{ipd} in the Weber–Morris equation. The rate constant for intraparticle diffusion k_{ipd} is determined by analyzing the slope of the linear equation established between the square root of time ($t^{1/2}$) and the amount of adsorbate adsorbed, based on the initial concentrations of the metal ions. Table 6 presents the intraparticle diffusion rate constant k_{ipd} and correlation coefficient R^2 derived from the intraparticle diffusion rate equation. The value of R^2 exceeds 0.9 which indicates that the adsorption of CV dye ions onto the nanoparticles occurred through the intraparticle diffusion mechanism.[65]

Table 6 Intra-particle diffusion kinetic model and Elovich kinetic model for CV dye adsorption onto FeO(B), FeO IL-1, and FeO IL-2 NPs

Intra-particle diffusion	Bare FeO	FeO-IL1	FeO-IL2
Intra-particle diffusion kinetic model			
K_{ipd} (mg g^{-1} min$^{-1/2}$)	1.36	1.07	1.12
C	30.64	29.98	29.88
R^2	0.91	0.87	0.93
Elovich kinetic model			
α (mg g^{-1} min^{-1})	22.63	102.05	65.26
β (g mg^{-1})	0.2272	0.2915	0.2744
R^2	0.76	0.70	0.80

Table 7 Kinetic parameters for adsorption of chromium

Kinetic models		Bare FeO
Pseudo first order	q_e (mg g^{-1})	8.1456
	K_1 (L mg^{-1})	−0.0000532
	R^2	0.91709
Pseudo second order	q_e (mg g^{-1})	12.3289
	q_e^2	152.00266
	K_2 (g mg^{-1} min^{-1})	0.082102
	R^2	0.99621
Intraparticle diffusion	K_i (mg g^{-1} min$^{-1/2}$)	6.07272
	X (mg g^{-1})	0.4943
	R^2	0.9521
Elovich	α (mg g^{-1} min^{-1})	0.55513
	β (g mg^{-1})	8.02681
	R^2	0.96042

3.5.5 Adsorption kinetics for chromium. The calculated values of the kinetic model are given in Table 7. A graphical representation of various kinetics models is shown in Fig. 15. The R^2 values of pseudo-first-order and pseudo-second-order were found to be 0.91709 and 0.99621. This indicates that the adsorption reaction fits better to the pseudo-second-order and the process of adsorption is chemical in nature. The values of K_1 and K_2 were found to be −0.0000532 and 0.082102; the higher value of K_2 validates that the adsorption process follows a pseudo-second-order model. The IPDM and Elovich model are also calculated and show that R^2 values were 0.95 and 0.96. The assumption of the Elovich model is built on the variation in the sorption energies of sites because of variations amongst these sorptive sites. From the equation of the Elovich model the value of α was found to be 0.55513 mg g^{-1} min^{-1} and β was 8.02681 g mg^{-1} (Fig. 15).

Table 8 Standard deviation for all the applied models for CV dye adsorption onto FeO(B), FeO IL-1, and FeO IL-2 NPs

Model	NPs type	Parameter type	N total	Standard deviation
Langmuir	FeO bare	$1/C_e$	6	0.60431
		$1/q_e$		0.01883
	FeO-IL1	$1/C_e$		2.92034
		$1/q_e$		0.01843
	FeO-IL2	$1/C_e$		1.51369
		$1/q_e$		0.01853
Freundlich	FeO bare	$\log C_e$	6	0.56018
		$\log q_e$		0.2646
	FeO-IL1	$\log C_e$		0.77561
		$\log q_e$		0.26678
	FeO-IL2	$\log C_e$		0.67028
		$\log q_e$		0.26735
Tempkin	FeO bare	$\ln C_e$	6	1.28986
		q_e		25.07089
	FeO-IL1	$\ln C_e$		1.78591
		q_e		26.20467
	FeO-IL2	$\ln C_e$		1.54337
		q_e		26.22259
Pseudo second order	FeO bare	t	5	42.95346
		t/q_t		3.14172
	FeO-IL1	t		42.95346
		t/q_t		2.60714
	FeO-IL2	t		42.95346
		t/q_t		2.67749
Intraparticle diffusion	FeO bare	$t^{1/2}$	5	2.88044
		q_t		4.10755
	FeO-IL1	$t^{1/2}$		2.88044
		q_t		3.29063
	FeO-IL2	$t^{1/2}$		2.88044
		q_t		3.33253
Elovich	FeO bare	$\ln t$	5	0.8448
		q_t		4.10755
	FeO-IL1	$\ln t$		0.8448
		q_t		3.29063
	FeO-IL2	$\ln t$		0.8448
		q_t		0.33253

3.6 Thermodynamic analysis

The thermodynamic investigation of the adsorption procedure aimed to assess the spontaneity and stability of the adsorbed phase. The study involved varying the temperature within the range of 10 to 60 °C while maintaining an initial dye concentration of 30 ppm, pH level of 10, and adsorbent dosage of 30 mg/30 mL. The experimental results revealed that the removal of dye increased with rising temperatures, suggesting that the adsorption process was endothermic. To comprehensively understand the thermodynamics of the system, the values of Gibbs energy ($\Delta G°$), entropy ($\Delta S°$), and enthalpy ($\Delta H°$) were scrutinized (Table 9). By employing relevant equations, the ΔG^0 for the adsorption process was calculated. The positive correlation between temperature and dye removal, coupled with the thermodynamic parameters, indicates that the adsorption of dye onto the adsorbent was a spontaneous and thermally favored process.

$$\Delta G^\circ = \Delta H^\circ - T\Delta S^\circ \quad (9)$$

where

$$\Delta G^\circ = -RT\ln K \quad (10)$$

T is absolute temperature (K), R is the universal gas constant, and K is the distribution coefficient for adsorption and is determined using the following equation.

$$K = q_e/C_e \quad (11)$$

The Langmuir isotherm section has previously covered parameters C_e and q_e. The thermodynamic parameters $\Delta H°$ and $\Delta S°$ were determined by analyzing the slope and intercept of the plot of $\Delta G°$ *versus* T. Notably, the calculated $\Delta G°$ values were negative, underscoring the viability and spontaneity of crystal violet (CV) adsorption on the IL-modified FeO. In the context of CV adsorption, the obtained $\Delta H°$ value was found to be positive, signifying the endothermic nature of the process and indicative of a physisorption phenomenon. This suggests that CV molecules were adsorbed onto the modified FeO surface in a manner where the distribution appeared more random, as indicated by the positive $\Delta S0$ value.[66]

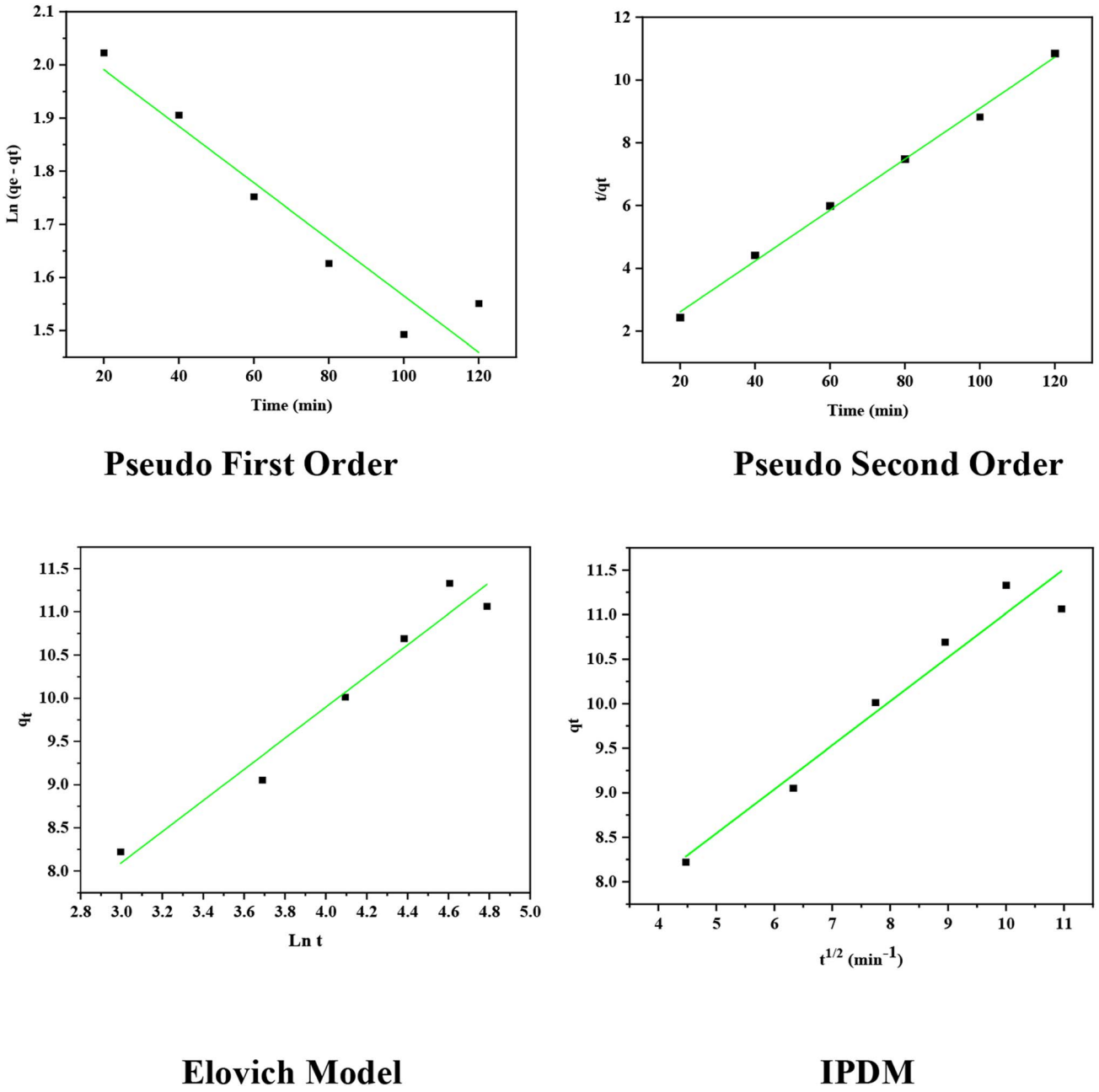

Fig. 15 Adsorption kinetics for Cr(VI) removal.

3.7 Reusability

3.7.1 Recycling of adsorbent for removal of CV dye. Subsequently, an examination was conducted to determine the impact of recycled NPs on the efficiency of dye decomposition. In order to investigate this phenomenon, the previously irradiated dye solution underwent centrifugation at a rate of 10000 rotations per minute for a duration of 30 minutes. This process was carried out to gather the NPs, which were then treated with washing with ethanol to eliminate the pre-existing loaded dye. Finally, the NPs were dried through desiccation. The recycled NP powder was utilised to irradiate the dye solution in an orbital shaker. In contrast to the original NP powder, there has been a reduction in the rate of degradation with each successive cycle (Fig. 16). The experiment was replicated five times utilising identical methodology, and it was found that in the second cycle bare-FeO, II-1, and IL-2 NPs show 88.87%, 95.79%, and 95.97% removal efficiency respectively due to blocking of the active site.

3.7.2 Recycling of adsorbent for removal of chromium. The regeneration study of the synthesized nanomaterials is represented in Fig. 17. A total of five regeneration cycles were performed using sodium hydroxide of 0.6 M to treat the adsorbent after each cycle. To investigate this phenomenon, the previously treated chromium solution underwent centrifugation at

Table 9 CV dye adsorption thermodynamic parameters

NP type	Temperature (°C)	$\Delta G°$ (kJ mol^{-1})	$\Delta H°$ (kJ mol^{-1})	$\Delta S°$ (J (mol^{-1} K^{-1}))
Bare FeO	10	−7262.16	13012.4	146.2433
	20	−7658.48		
	30	−8027.92		
	40	−8181.24		
	50	−8353.63		
	60	−8458.09		
FeO-IL1	10	−8317.31	20042.8	409.1319
	20	−9168.95		
	30	−9761.55		
	40	−9874.27		
	50	−9950.59		
	60	−10031.4		
FeO-IL2	10	−6798.99	27902.8	281.255
	20	−7557.95		
	30	−8456.76		
	40	−8432.92		
	50	−8375.63		
	60	−8331.91		

a rate of 5000 rotations per minute for a duration of 20 minutes and were then washed with 0.6 M sodium hydroxide. Finally, the NPs were dried using a hot air oven. The removal efficiency of chromium with fresh nanomaterials was as follows: bare FeO (68.50%), FeOIL-1 (72.85%), and FeOIL-2 (77.21%), whereas its removal efficiency decreased with each regeneration cycle. From the results, it is concluded that the reusability of the adsorbent is cost-effective and efficient for up to three cycles.

4. Adsorption mechanism

A number of mechanisms regulate adsorption on the surface of NPs. The functionalization of NPs is extremely important in the adsorption process. The FTIR spectrum of all synthesized NPs reveals the existence of –OH groups in aromatic and aliphatic form which leads to the adsorption of dye. Fig. 18(a) depicts the FT-IR spectrum of the nano adsorbents following CV dye loading. The new peaks that appeared at 2924.01 cm^{-1}, 2926.2 cm^{-1} and 2923.19 cm^{-1} represent the C–H bonding of alkane groups having sp^3 hybridization and bending of the carboxyl group's O–H bond stretching modes, whereas a further peak at 2853.6 cm^{-1} represents the weak C–H bonding in aldehyde groups with sp^3 hybridization. As illustrated in Fig. 18, the small peaks seen at 1626.75 cm^{-1}, 1618.39 cm^{-1}, and 1623.15 cm^{-1} indicate the saturated amide group having CO bonding. These aforementioned peak patterns validate the CV dye adsorption on iron oxide nano-adsorbents prepared with bare and ionic liquids.[67,68]

CV dye is categorized as a cationic dye due to its positive charge, while FeO nanoparticles typically acquire negatively charged surfaces following modification with hydrophobic ionic liquids (ILs). Interfaces between water and apolar media incur a significant free energy cost, leading to recombination to minimize the total interfacial area. In water, recombination occurs after collisions. The adsorption of amphiphilic molecules, whether ionic or non-ionic, macromolecules, or

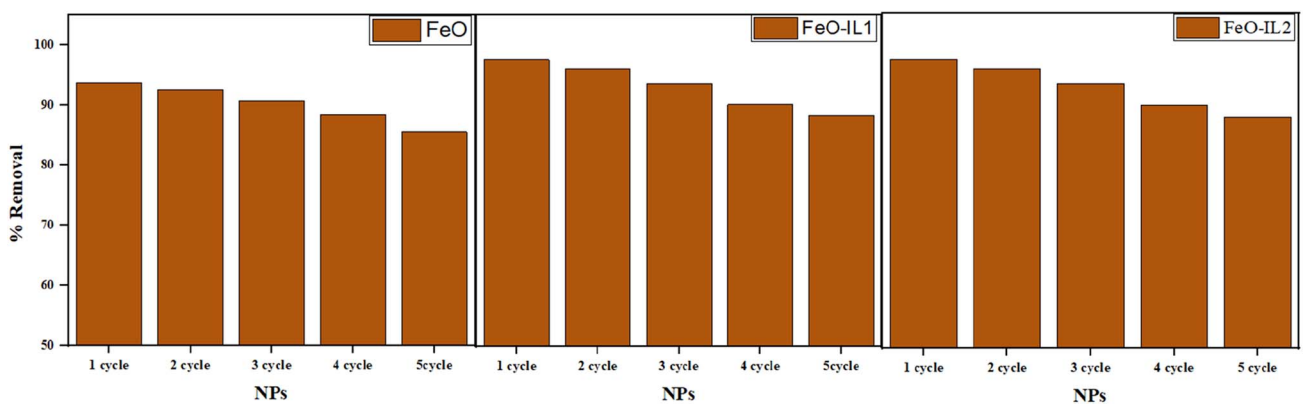

Fig. 16 Reusability graphs for the adsorbents used for CV dye removal.

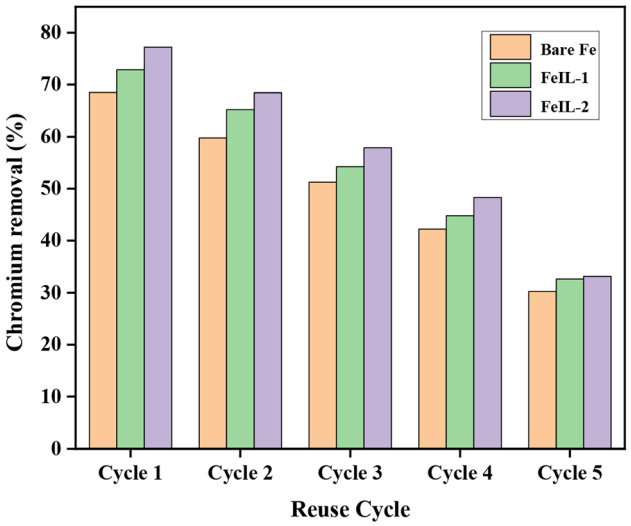

Fig. 17 Reusability graphs for the adsorbents used for Cr(VI) removal.

particles, hinders recombination, resulting in the metastability of emulsions, foams, and polymer dispersions. In surfactant-free emulsions, droplets are ionized and possess a negative electrical charge. The interaction between water and air yields similar outcomes.[69] Furthermore, the negative charge increases rapidly with pH and the total concentration of hydroxide ions.

The electrostatic attraction between the positively charged CV dye and the negatively charged nanoparticle surface facilitates the adsorption process (refer to Fig. 18(b)). Additionally, nanoparticles offer a high surface area-to-volume ratio, providing numerous sites for dye molecule adsorption.[70] Synthesized nanoparticles often feature surface functional groups capable of interacting with CV dye through chemical bonding or coordination. For instance, if the nanoparticle surface contains imide groups, hydroxyl (–OH) groups, or amino ($–NH_2$) groups, these functional groups can form hydrogen bonds or coordinate with the CV dye and Cr(VI) molecules, promoting their adsorption onto the nanoparticle surface (see Fig. 18(b)). Furthermore, ionic liquids (ILs) effectively stabilize nanoparticles, preventing agglomeration by leveraging their size and charge characteristics. These properties makes ILs valuable for controlling the morphology and phase of inorganic nanomaterials.[71]

In summary, the adsorption of CV dye[72] and Cr(VI)[73] onto nanoparticles is driven by electrostatic attraction between the positively charged dye and heavy metal and the negatively charged nanoparticle surface. The substantial surface area of nanoparticles facilitates adsorption, while surface functional

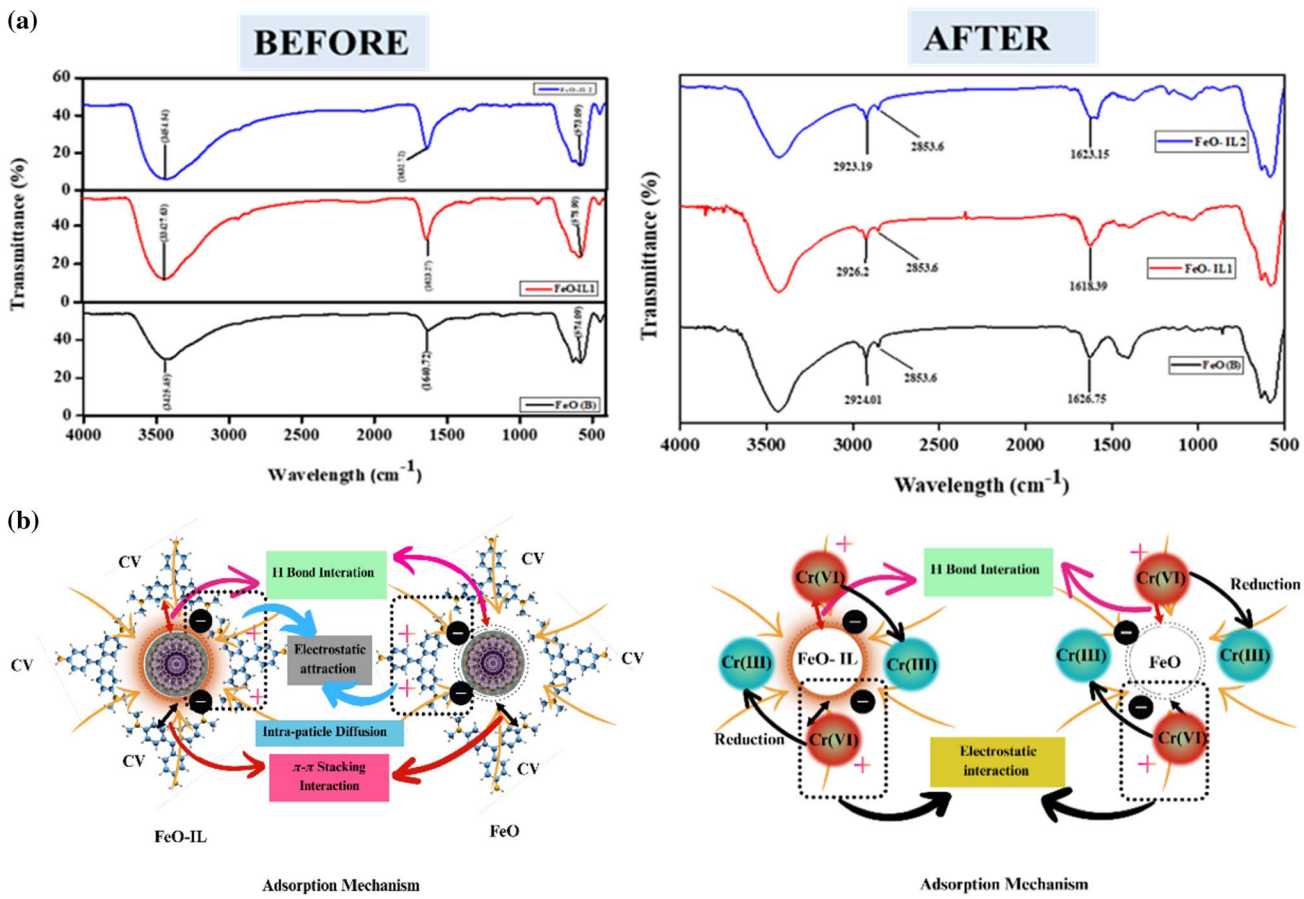

Fig. 18 (a) FTIR spectra showing the loading of dye on the synthesized NPs. (b) Pictorial representation of the adsorption mechanism of dye and heavy metal.

groups on nanoparticles and the stabilizing effects of ILs contribute to the adsorption process through chemical bonding, coordination, and size control.[74]

5. Conclusion

Various techniques were employed to efficiently eliminate CV dye from aqueous solutions utilising both bare and ionic liquid (IL)-modified iron oxide nanoparticles (FeO NPs) synthesized in this investigation. The IL-modified crystalline FeO NPs were observed to be smaller in size compared to their unmodified counterparts which means the ionic liquid acts as a good reducing agent as well as stabilizing and capping agent. The surface modification of the NPs with IL did not solely control their size, but nonetheless enhanced their capacity to act as an adsorbent. Using an orbital shaker, the adsorption efficiency of the NPs using batch mode was tested. In the CV dye removal study at pH 10 using a 30 mg dose of nanoparticles for 60 min was found to be the most optimised conditions. The results indicated that the adsorption efficiency of the dye increased as the NP dosage increased, while it decreased with an increase in the concentration of CV dye or Cr(VI). The adsorption of the dye onto both unmodified and IL-modified NPs followed a pseudo-second-order kinetic model, and three distinct adsorption isotherms were used to elucidate the mechanism and rate of the adsorption process. The Langmuir and Temkin isotherm models agreed well with the experimental results, indicating monolayer adsorption of the CV dye and Cr(VI) on nanoparticle surfaces, with the Langmuir model offering a better match ($R^2 = 0.99$). With strong R^2 values (0.93–0.97) and large q_e values (22.07–24.41 mg g^{-1}) for bare and IL-coated nanoparticles, pseudo-second-order kinetics was useful in characterising the adsorption process, underlining the relevance of this model for the investigation. The linear fit seen in the graphical depiction of the intraparticle diffusion model, with R^2 greater than 0.9, supports the model's efficacy in capturing the adsorption process. This result clearly shows that CV dye ion adsorption on nanoparticles happens primarily *via* the intraparticle diffusion process. Furthermore, we conducted a comparative analysis of all three types of NPs and ILs under consistent conditions: pH 6, 100 minutes of contact time, 40 ppm Cr metal concentration, 170 mg NP dosage, and 60 °C for the Cr(VI) metal removal. It was established that the ILs can effectively modify the NPs to enhance their suitability for the removal of CV dye and Cr(VI) from water.

In conclusion, the synthesis of IL-modified FeO NPs through microwave irradiation proved to be a promising approach for efficient removal of CV dye and Cr(VI) from aqueous solutions. These findings contribute to the understanding of the adsorption mechanisms and highlight the potential applications of these NPs in wastewater treatment for addressing the environmental challenges posed by industrial effluents. However, further research is needed to optimize and scale up the synthesis process, investigate regeneration methods for sustainable use, and explore the potential for real-world applications in diverse industrial settings.

Conflicts of interest

There are no conflicts to declare.

Acknowledgements

The authors would like to express their deep gratefulness to the University Grants Commission-BSR Start-up Research grant (UGC-BSR) for generously granting the essential financial backing. The grant's sanction letter is identified by the number F.30-490/2019 (BSR).

References

1 A. Inyinbor Adejumoke, O. Adebesin Babatunde, P. Oluyori Abimbola, A. Adelani Akande Tabitha, O. Dada Adewumi and A. Oreofe Toyin, Water pollution: effects, prevention, and climatic impact, *Water Challenges of an Urbanizing World*, 2018, **33**, 33–47.

2 J. Vasa, A. Aggarwal and M. Rebernik, Problem and prospectus of SME sectors in India & China with special reference to chemical, pharma and textile industries, *Int. J. Sci. Eng. Res.*, 2014, **5**(2), 395–407.

3 S. Mani and R. N. Bharagava, Textile industry wastewater: environmental and health hazards and treatment approaches, in *Recent Advances in Environmental Management*, CRC Press, 2018, pp. 47–69.

4 M. Yasasve, M. Manjusha, D. Manojj, N. M. Hariharan, P. S. Preethi, P. Asaithambi, N. Karmegam and M. Saravanan, Unravelling the emerging carcinogenic contaminants from industrial waste water for prospective remediation by electrocoagulation–a review, *Chemosphere*, 2022, 136017.

5 S. S. Affat, Classifications, advantages, disadvantages, toxicity effects of natural and synthetic dyes: A review, *University of Thi-Qar Journal of Science*, 2021, **8**(1), 130–135.

6 R. Kishor, D. Purchase, G. D. Saratale, R. G. Saratale, L. F. Ferreira, M. Bilal, R. Chandra and R. N. Bharagava, Ecotoxicological and health concerns of persistent coloring pollutants of textile industry wastewater and treatment approaches for environmental safety, *J. Environ. Chem. Eng.*, 2021, **9**(2), 105012.

7 T. Rasheed, S. Shafi, M. Bilal, T. Hussain, F. Sher and K. Rizwan, Surfactants-based remediation as an effective approach for removal of environmental pollutants—A review, *J. Mol. Liq.*, 2020, **318**, 113960.

8 A. S. Ayangbenro and O. O. Babalola, A new strategy for heavy metal polluted environments: a review of microbial biosorbents, *Int. J. Environ. Res. Public Health*, 2017, **14**(1), 94.

9 S. Velusamy, A. Roy, S. Sundaram and T. Kumar Mallick, A review on heavy metal ions and containing dyes removal through graphene oxide-based adsorption strategies for textile wastewater treatment, *Chem. Rec.*, 2021, **21**(7), 1570–1610.

10 C. Verma, E. E. Ebenso and M. A. Quraishi, Transition metal nanoparticles in ionic liquids: Synthesis and stabilization, *J. Mol. Liq.*, 2019, **276**, 826–849.

11 J. Riu, I. Schönsee, D. Barcelo and C. Rafols, Determination of sulphonated azo dyes in water and wastewater, *TrAC, Trends Anal. Chem.*, 1997, **16**(7), 405–419.
12 G. Tjandraatmadja, C. Diaper, Y. Gozukara, L. Burch, C. Sheedy and G. Price, Sources of critical contaminants in domestic wastewater: contaminant contribution from household products, *Report for the CSIRO: Water for a Healthy Country National Research Flagship*, 2008.
13 A. K. Choudhury, Eco-friendly dyes and dyeing, *Adv. Mater. Technol. Environ.*, 2018, **2**, 145–176.
14 B. Ates, S. Koytepe, A. Ulu, C. Gurses and V. K. Thakur, Chemistry, structures, and advanced applications of nanocomposites from biorenewable resources, *Chem. Rev.*, 2020, **120**(17), 9304–9362.
15 Y. Zou, X. Wang, A. Khan, P. Wang, Y. Liu, A. Alsaedi, T. Hayat and X. Wang, Environmental remediation and application of nanoscale zero-valent iron and its composites for the removal of heavy metal ions: a review, *Environ. Sci. Technol.*, 2016, **50**(14), 7290–7304.
16 I. Y. El-Sherif, S. Tolani, K. Ofosu, O. A. Mohamed and A. K. Wanekaya, Polymeric nanofibers for the removal of Cr (III) from tannery waste water, *J. Environ. Manage.*, 2013, **129**, 410–413.
17 Y. Zou, X. Wang, A. Khan, P. Wang, Y. Liu, A. Alsaedi, T. Hayat and X. Wang, Environmental remediation and application of nanoscale zero-valent iron and its composites for the removal of heavy metal ions: a review, *Environ. Sci. Technol.*, 2016, **50**(14), 7290–7304.
18 S. Mani and R. N. Bharagava, Exposure to crystal violet, its toxic, genotoxic and carcinogenic effects on environment and its degradation and detoxification for environmental safety, *Reviews of Environmental Contamination and Toxicology*, vol. 237, 2016, pp. 71–104.
19 N. Sharma, K. K. Sodhi, M. Kumar and D. K. Singh, Heavy metal pollution: Insights into chromium eco-toxicity and recent advancement in its remediation, *Environ. Nanotechnol., Monit. Manage.*, 2021, **15**, 100388.
20 S. I. Selvam, R. I. Mala and V. Muthukakshmi, A hydrochemical analysis and evaluation of groundwater quality index in Thoothukudi district, Tamilnadu, South India, *Int. J. Adv. Eng. Appl.*, 2013, **2**(3), 25–37.
21 T. Naseem and T. Durrani, The role of some important metal oxide nanoparticles for wastewater and antibacterial applications: A review, *Environ. Chem. Ecotoxicol.*, 2021, **3**, 59–75.
22 L. Wang, C. Shi, L. Pan, X. Zhang and J. J. Zou, Rational design, synthesis, adsorption principles and applications of metal oxide adsorbents: a review, *Nanoscale*, 2020, **12**(8), 4790–4815.
23 X. Chen, Z. Wu, D. Liu and Z. Gao, Preparation of ZnO photocatalyst for the efficient and rapid photocatalytic degradation of azo dyes, *Nanoscale Res. Lett.*, 2017, **12**, 1–10.
24 E. Ghasemian and Z. Palizban, Comparisons of azo dye adsorptions onto activated carbon and silicon carbide nanoparticles loaded on activated carbon, *Int. J. Environ. Sci. Technol.*, 2016, **13**, 501–512.
25 M. A. Mazmanci, Decolorization of azo dyes by immobilized fungi, *Biodegradation of azo dyes*, 2010, pp. 169–181.
26 U. O. Aigbe, R. Das, W. H. Ho, V. Srinivasu and A. Maity, A novel method for removal of Cr (VI) using polypyrrole magnetic nanocomposite in the presence of unsteady magnetic fields, *Sep. Purif. Technol.*, 2018, **194**, 377–387.
27 V. Katheresan, J. Kansedo and S. Y. Lau, Efficiency of various recent wastewater dye removal methods: A review, *J. Environ. Chem. Eng.*, 2018, **6**(4), 4676–4697.
28 S. Khurshid, Z. Gul, J. Khatoon, M. R. Shah, I. Hamid, I. A. Khan and F. Aslam, Anionic azo dyes removal from water using amine-functionalized cobalt–iron oxide nanoparticles: a comparative time-dependent study and structural optimization towards the removal mechanism, *RSC Adv.*, 2020, **10**(2), 1021–1041.
29 P. Benjwal, M. Kumar, P. Chamoli and K. K. Kar, Enhanced photocatalytic degradation of methylene blue and adsorption of arsenic (iii) by reduced graphene oxide (rGO)–metal oxide (TiO2/Fe3O4) based nanocomposites, *RSC Adv.*, 2015, **5**(89), 73249–73260.
30 I. Mironyuk, T. Tatarchuk, M. Naushad, H. Vasylyeva and I. Mykytyn, Highly efficient adsorption of strontium ions by carbonated mesoporous TiO2, *J. Mol. Liq.*, 2019, **285**, 742–753.
31 E. Y. Shaba, J. O. Jacob, J. O. Tijani and M. A. Suleiman, A critical review of synthesis parameters affecting the properties of zinc oxide nanoparticle and its application in wastewater treatment, *Appl. Water Sci.*, 2021, **11**, 1–41.
32 N. Durán, P. D. Marcato, G. I. De Souza, O. L. Alves and E. Esposito, Antibacterial effect of silver nanoparticles produced by fungal process on textile fabrics and their effluent treatment, *J. Biomed. Nanotechnol.*, 2007, **3**(2), 203–208.
33 D. Devi, N. M. Julkapli, S. Sagadevan and M. R. Johan, Eco-friendly green synthesis approach and evaluation of environmental and biological applications of Iron oxide nanoparticles, *Inorg. Chem. Commun.*, 2023, 110700.
34 M. Kaur and N. Kaur, Ferrites: synthesis and applications for environmental remediation, in *Ferrites and Ferrates: Chemistry and Applications in Sustainable Energy and Environmental Remediation*, American Chemical Society, 2016, pp. 113–136.
35 Y. L. Zhu, Y. Katayama and T. Miura, Electrochemical preparation of nickel and iron nanoparticles in a hydrophobic ionic liquid, *Electrochem. Solid-State Lett.*, 2011, **14**(12), D110.
36 D. Raut, K. Wankhede, V. Vaidya, S. Bhilare, N. Darwatkar, A. Deorukhkar, G. Trivedi and M. Salunkhe, Copper nanoparticles in ionic liquids: Recyclable and efficient catalytic system for 1, 3-dipolar cycloaddition reaction, *Catal. Commun.*, 2009, **10**(8), 1240–1243.
37 F. A. Yassin, F. Y. El Kady, H. S. Ahmed, L. K. Mohamed, S. A. Shaban and A. K. Elfadaly, Highly effective ionic liquids for biodiesel production from waste vegetable oils, *Egypt. J. Pet.*, 2015, **24**(1), 103–111.
38 S. Chaudhary, Y. Kaur, A. Umar and G. R. Chaudhary, Ionic liquid and surfactant functionalized ZnO nanoadsorbent for

recyclable proficient adsorption of toxic dyes from waste water, *J. Mol. Liq.*, 2016, **224**, 1294–1304.

39 K. Nain, D. Dhillayan, S. Bansal, Q. Hundal, P. Saharan and S. Bhukal, Adsorption potential of ionic liquid-modified ZnO nanoparticles for highly efficient removal of azo dye: detailed isotherms and kinetics, *Environ. Sci. Pollut. Res.*, 2023, 1–7.

40 Z. Alhalili, Green synthesis of copper oxide nanoparticles CuO NPs from Eucalyptus globulus leaf extract: adsorption and design of experiments, *Arabian J. Chem.*, 2022, **15**(5), 103739.

41 Y. M. Mohamed and Y. A. Attia, Nano Pt/TiO2 photocatalyst for ultrafast production of sulfamic acid derivatives using 4-nitroacetanilides as nitrogen precursor in continuous flow reactors, *Environ. Sci. Pollut. Res.*, 2023, **30**(17), 51344–51355.

42 L. C. Gonçalves, A. B. Seabra, M. T. Pelegrino, D. R. De Araujo, J. S. Bernardes and P. S. Haddad, Superparamagnetic iron oxide nanoparticles dispersed in Pluronic F127 hydrogel: potential uses in topical applications, *RSC Adv.*, 2017, 7(24), 14496–14503.

43 A. Gouthaman, A. Gnanaprakasam, V. M. Sivakumar, M. Thirumarimurugan, M. A. Ahamed and R. S. Azarudeen, Enhanced dye removal using polymeric nanocomposite through incorporation of Ag doped ZnO nanoparticles: Synthesis and characterization, *J. Hazard. Mater.*, 2019, **373**, 493–503.

44 F. C. Oliveira, F. B. Effenberger, M. H. Sousa, R. F. Jardim, P. K. Kiyohara, J. Dupont, J. C. Rubim and L. M. Rossi, Ionic liquids as recycling solvents for the synthesis of magnetic nanoparticles, *Phys. Chem. Chem. Phys.*, 2011, **13**(30), 13558–13564.

45 S. W. Hwang, A. Umar, G. N. Dar, S. H. Kim and R. I. Badran, Synthesis and characterization of iron oxide nanoparticles for phenyl hydrazine sensor applications, *Sens. Lett.*, 2014, **12**(1), 97–101.

46 Z. N. Kayani, S. Arshad, S. Riaz and S. Naseem, Synthesis of iron oxide nanoparticles by sol–gel technique and their characterization, *IEEE Trans. Magn.*, 2014, **50**(8), 1–4.

47 T. Gutel, C. C. Santini, K. Philippot, A. Padua, K. Pelzer, B. Chaudret, Y. Chauvin and J. M. Basset, Organized 3D-alkyl imidazolium ionic liquids could be used to control the size of in situ generated ruthenium nanoparticles?, *J. Mater. Chem.*, 2009, **19**(22), 3624–3631.

48 G. Clavel, J. Larionova, Y. Guari and C. Guérin, Synthesis of cyano-bridged magnetic nanoparticles using room-temperature ionic liquids, *Chem.–Eur. J.*, 2006, **12**(14), 3798–3804.

49 C. V. Rigueto, J. S. Piccin, A. Dettmer, M. Rosseto, G. L. Dotto, A. P. de Oliveira Schmitz, D. Perondi, T. S. de Freitas, R. A. Loss and C. A. Geraldi, Water hyacinth (Eichhornia crassipes) roots, an amazon natural waste, as an alternative biosorbent to uptake a reactive textile dye from aqueous solutions, *Ecol. Eng.*, 2020, **150**, 105817.

50 S. M. Shalaby, F. F. Madkour, H. Y. El-Kassas, A. A. Mohamed and A. M. Elgarahy, Green synthesis of recyclable iron oxide nanoparticles using Spirulina platensis microalgae for adsorptive removal of cationic and anionic dyes, *Environ. Sci. Pollut. Res.*, 2021, **28**, 65549–65572.

51 F. Marrakchi, B. H. Hameed and E. H. Hummadi, Mesoporous biohybrid epichlorohydrin crosslinked chitosan/carbon–clay adsorbent for effective cationic and anionic dyes adsorption, *Int. J. Biol. Macromol.*, 2020, **163**, 1079–1086.

52 M. A. Barakat, R. Kumar, M. K. Seliem, A. Q. Selim, M. Mobarak, I. Anastopoulos, D. Giannakoudakis, M. Barczak, A. Bonilla-Petriciolet and E. A. Mohamed, Exfoliated clay decorated with magnetic iron nanoparticles for crystal violet adsorption: modeling and physicochemical interpretation, *Nanomaterials*, 2020, **10**(8), 1454.

53 P. L. Kiew, N. A. Fauzi, S. A. Firdiani, M. K. Lam, L. S. Tan and W. M. Yeoh, Iron oxide nanoparticles derived from Chlorella vulgaris extract: Characterization and crystal violet photodegradation studies, *Prog. Energy Environ.*, 2023, 1.

54 M. H. Sayadi, N. Salmani, A. Heidari and M. R. Rezaei, Bio-synthesis of palladium nanoparticle using Spirulina platensis alga extract and its application as adsorbent, *Surf. Interfaces*, 2018, **10**, 136–143.

55 J. Hu, G. Chen and I. M. Lo, Removal and recovery of Cr (VI) from wastewater by maghemite nanoparticles, *Water Res.*, 2005, **39**(18), 4528–4536.

56 J. Hu, G. Chen and I. M. Lo, Removal and recovery of Cr (VI) from wastewater by maghemite nanoparticles, *Water Res.*, 2005, **39**(18), 4528–4536.

57 V. Arumugam, K. G. Moodley, A. Dass, R. M. Gengan, D. Ali, S. Alarifi, M. Chandrasekaran and Y. Gao, Ionic liquid covered iron-oxide magnetic nanoparticles decorated zeolite nanocomposite for excellent catalytic reduction and degradation of environmental toxic organic pollutants and dyes, *J. Mol. Liq.*, 2021, **342**, 117492.

58 A. M. Rabie, H. M. Abd El-Salam, M. A. Betiha, H. H. El-Maghrabi and D. Aman, Mercury removal from aqueous solution via functionalized mesoporous silica nanoparticles with the amine compound, *Egypt. J. Pet.*, 2019, **28**(3), 289–296.

59 D. Balarak, H. Azarpira and F. K. Mostafapour, Thermodynamics of removal of cadmium by adsorption on Barley husk biomass, *Pharma Chem.*, 2016, **8**(10), 243–247.

60 E. Bazrafshan, M. Sobhanikia, F. K. Mostafapour, H. Kamani and D. Balarak, Chromium biosorption from aqueous environments by mucilaginous seeds of Cydonia oblonga: kinetic and thermodynamic studies, *Global NEST J.*, 2017, **19**(2), 269–277.

61 D. Balarak, A. Joghataei, H. Azarpira and F. K. Mostafapour, Isotherms and thermodynamics of Cd (II) ion removal by adsorption onto Azolla filiculoides, *Int. J. Pharm. Technol.*, 2016, **8**(3), 15780–15788.

62 H. Azarpira, Y. Mahdavi and D. Balarak, Removal of Cd (II) by adsorption on agricultural waste biomass, *Pharma Chem.*, 2016, **8**(12), 61–67.

63 S. Agarwal, I. Tyagi, V. K. Gupta, M. H. Dehghani, J. Jaafari, D. Balarak and M. Asif, Rapid removal of noxious nickel (II) using novel γ-alumina nanoparticles and multiwalled

carbon nanotubes: kinetic and isotherm studies, *J. Mol. Liq.*, 2016, **224**, 618–623.

64 N. Hasani, T. Selimi, A. Mele, V. Thaçi, J. Halili, A. Berisha and M. Sadiku, Theoretical, equilibrium, kinetics and thermodynamic investigations of methylene blue adsorption onto lignite coal, *Molecules*, 2022, **27**(6), 1856.

65 M. Manjuladevi, R. Anitha and S. J. Manonmani, Kinetic study on adsorption of Cr (VI), Ni (II), Cd (II) and Pb (II) ions from aqueous solutions using activated carbon prepared from Cucumis melo peel, *Appl. Water Sci.*, 2018, 1–8.

66 S. Chander, S. Yadav, A. Gupta and N. Luhach, Sequestration of Ni (II), Pb (II), and Zn (II) utilizing biogenic synthesized Fe3O4/CLPC NCs and modified Fe3O4/CLPC@ CS NCs: Process optimization, simulation modeling, and feasibility study, *Environ. Sci. Pollut. Res.*, 2023, 1–22.

67 A. M. Elgarahy, K. Z. Elwakeel, G. A. Elshoubaky and S. H. Mohammad, Microwave-accelerated sorption of cationic dyes onto green marine algal biomass, *Environ. Sci. Pollut. Res.*, 2019, **26**, 22704–22722.

68 S. Bhukal, A. Sharma, D. Rishi, S. Kumar, B. Deepak, K. Pal and S. Mona, Spirulina based iron oxide nanoparticles for adsorptive removal of crystal violet dye, *Top. Catal.*, 2022, **65**(19–20), 1675–1685.

69 R. Foroutan, S. J. Peighambardoust, S. H. Peighambardoust, M. Pateiro and J. M. Lorenzo, Adsorption of crystal violet dye using activated carbon of lemon wood and activated carbon/Fe3O4 magnetic nanocomposite from aqueous solutions: a kinetic, equilibrium and thermodynamic study, *Molecules*, 2021, **26**(8), 2241.

70 T. Rasheed, Magnetic nanomaterials: Greener and sustainable alternatives for the adsorption of hazardous environmental contaminants, *J. Cleaner Prod.*, 2022, **362**, 132338.

71 S. Ravula, S. N. Baker, G. Kamath and G. A. Baker, Ionic liquid-assisted exfoliation and dispersion: stripping graphene and its two-dimensional layered inorganic counterparts of their inhibitions, *Nanoscale*, 2015, **7**(10), 4338–4353.

72 M. A. Barakat, R. Kumar, M. K. Seliem, A. Q. Selim, M. Mobarak, I. Anastopoulos, D. Giannakoudakis, M. Barczak, A. Bonilla-Petriciolet and E. A. Mohamed, Exfoliated clay decorated with magnetic iron nanoparticles for crystal violet adsorption: modeling and physicochemical interpretation, *Nanomaterials*, 2020, **10**(8), 1454.

73 L. Tang, G. D. Yang, G. M. Zeng, Y. Cai, S. S. Li, Y. Y. Zhou, Y. Pang, Y. Y. Liu, Y. Zhang and B. Luna, Synergistic effect of iron doped ordered mesoporous carbon on adsorption-coupled reduction of hexavalent chromium and the relative mechanism study, *Chem. Eng. J.*, 2014, **239**, 114–122.

74 R. Mittal, A. Sharma, A. K. Bhardwaj, R. Bhateria, S. Bansal, R. Kashyap and S. Bhukal, Removal of Chromium (VI) using Spirulina assisted Synthesized Mesoporous Iron Oxide Nanoparticles, *Inorg. Chem. Commun.*, 2023, 110881.